ABSTRACT

Title of Dissertation: ACCELERATING MATERIALS DISCOVERY WITH COMPUTATION: HUMAN-IN-THE-LOOP, QUANTUM MACHINE LEARNING, AND FIRST PRINCIPLES COMPUTATION

Felix Adams
Doctor of Philosophy, 2026

Dissertation Directed by: Professors Yifei Mo and Ichiro Takeuchi
Department of Materials Science and Engineering

The central challenge of materials science is discovering and developing new materials that solve engineering challenges and enable new technologies. This thesis comprises three projects exploring the application of different computational techniques to materials discovery. The first project applied human-machine learning collaboration to autonomous experimentation. By presenting a human expert with a machine learning model's predictions and allowing them to provide their feedback, the performance and interpretability of the autonomous experiment was improved. The second project applied quantum kernel machine learning to x-ray diffraction pattern analysis. Comparing x-ray diffraction patterns using a quantum computer reduced the amount of experimental data needed to train machine learning models for some specific machine learning tasks similar to those in autonomous materials science. The third project applied high-throughput density functional theory calculations to the identification of novel candidate phase change materials. Using a first-principles thermodynamic approach, several promising materials systems were identified. These projects represent a sample of the future of computational materials discovery.

# ACCELERATING MATERIALS DISCOVERY WITH COMPUTATION: HUMAN-IN-THE-LOOP, QUANTUM MACHINE LEARNING, AND FIRST PRINCIPLES COMPUTATION

by

Felix Adams

Dissertation submitted to the Faculty of the Graduate School of the
University of Maryland, College Park in partial fulfillment
of the requirements for the degree of
Doctor of Philosophy
2026

Advisory Committee:
Professor Yifei Mo, Co-Chair/Advisor
Professor Ichiro Takeuchi, Co-Chair/Advisor
Dr. A. Gilad Kusne
Professor Carlos Ríos Ocampo
Professor Peter Chung

# Acknowledgments

I'm especially grateful for...

Alex Hall
Amanda Siciliano
Austin McDannald
Ben Watkins
Bryson Clifford
Carlos Ríos Ocampo
Charlie Schwarz
Chih-Yu Lee
Daiwei Zhu
Daniela Fontecha
David W. Steuerman
Evan Bearman
A. Gilad Kusne
Haotong Liang
The Hyattsville Figure Drawing Group
Ichiro Takeuchi
John Hoerauf
Kiyan Amirian
Liangbing Hu
Rachel Beall
Ramanuja Srinivasan Saravanan
Ryan Paxson
Ryan Kim
Sam Freed
The Staff of the UMD MSE Department
Ștefan Theodoru
Yifei Mo

...and so many others.

# Table of Contents


Acknowledgements ii

Table of Contents iii

Chapter 1: Introduction to Materials Discovery 1

Chapter 2: Human-in-the-Loop for Bayesian Autonomous Materials Phase Mapping 4
- 2.1 Abstract . . . 4
- 2.2 Introduction . . . 5
- 2.3 Results and Discussion . . . 10
- 2.4 Conclusion . . . 16
- 2.5 Methods . . . 16
  - 2.5.1 Autonomous phase-mapping algorithm . . . 17
  - 2.5.2 Human input integration . . . 19
  - 2.5.3 Phase region and phase boundary inputs . . . 21
  - 2.5.4 Region of interest input . . . 23
  - 2.5.5 Integrated workflow . . . 24
  - 2.5.6 Evaluating human-in-the-loop performance . . . 25
- 2.6 Original Author Contributions . . . 26

Chapter 3: Quantum Kernel Machine Learning for Autonomous Materials Science 27
- 3.1 Abstract . . . 27
- 3.2 Introduction . . . 28
- 3.3 Methods . . . 33
  - 3.3.1 XRD Dataset . . . 33
  - 3.3.2 Classical and Quantum Kernels for Autonomous Materials Science . . . 34
  - 3.3.3 Evaluating Quantum Kernel Performance . . . 37
- 3.4 Results and Discussion . . . 42
  - 3.4.1 Kernel Matrix Values . . . 42
  - 3.4.2 Model Complexities and Performance . . . 45
- 3.5 Conclusion . . . 49
- 3.6 Original Author Contributions . . . 50

Chapter 4: First-Principles Thermodynamic Analysis of Ternary Chalcogenide Phase Change Materials 51
4.1 Abstract . . . 51
4.2 Introduction . . . 52
4.3 Results . . . 54
4.3.1 Generation of Candidate Materials . . . 55
4.3.2 GST Polymorph Structures and Energies . . . 56
4.3.3 Telluride Mixtures . . . 57
4.3.4 Selenide Mixtures . . . 63
4.3.5 Multi-Anion Mixtures . . . 68
4.4 Discussion . . . 69
4.5 Methods . . . 72
4.5.1 Candidate Binary Selection . . . 72
4.5.2 Vacancy Charge Compensation . . . 73
4.5.3 Ternary Structure Ordering . . . 74
4.5.4 DFT Calculations . . . 75
4.6 Original Author Contributions . . . 75

Chapter 5: Summary and Future Work 76
5.1 Summary . . . 76
5.2 Future Work . . . 77

Publications 78

Appendix A: Supplemental Information for Quantum Kernel Machine Learning for Autonomous Materials Science 79
A.1 Calculation of Model Complexity and Geometric Difference . . . 79
A.2 Construction of Engineered Labels . . . 79
A.3 Kernel Matrices and Performance Data Replots . . . 80

Appendix B: Supplemental Information for First-Principles Thermodynamic Analysis of Ternary Chalcogenide Phase Change Materials 85
B.1 Results for Additional Select Mixtures . . . 85
B.1.1 In – Se Mixtures . . . 85
B.1.2 Miscellaneous Mixtures . . . 87

Bibliography 88

# Chapter 1: Introduction to Materials Discovery

New materials are essential for addressing engineering problems and enabling new technologies. However, discovering useful materials is challenging because of the extremely large accessible materials design space, spanning compositions, structures, synthesis conditions, and processing history. With each additional synthesis or processing parameter, such as temperature, time, concentration, pressure, etc., the combinatorial number of possible materials grows exponentially. This motivates the development of methods for efficiently searching this large, complex materials space.

There have been significant advances in the methods for materials discovery over time [1]. Traditional trial-and-error methods are not well suited for the vast and high-dimensional space accessible in modern materials science. Advances in computational methods, such as those based on first principles, have enabled the prediction of materials' properties before synthesis, but such calculations remain computationally expensive for many properties and are not always sufficiently accurate to direct materials selection. Current materials discovery techniques use data-driven approaches that combine high-throughput experiments and machine learning to generate and analyze large amounts of materials data [2].

High-throughput experiments and computation greatly accelerate the generation of materials science data and enable the transition to data-driven materials discovery [2, 3]. In high-throughput experiments, many compositions are synthesized and characterized at once or in parallel, often through composition spreads or multiplexed sample formats [3]. This enables the rapid mapping of composition-property relationships across broad materials spaces. High-throughput computation leverages supercomputing to predict the properties of a large num-

ber of materials beyond what can be studied experimentally [4]. These techniques create large databases that form the basis of data-driven materials discovery.

Autonomous experimentation represents a further step in this materials discovery paradigm integrating machine learning and automation to iteratively select and perform the most informative experiments [5]. In a typical autonomous workflow, a model is trained on the available experimental data and then used to choose the next experiment according to a specified utility criterion [6]. Automated instrumentation performs the selected measurement, the dataset is updated, and the cycle repeats. By focusing on the most informative measurements, autonomous experimentation can reduce the number of experiments needed to characterize a material system compared with uniform-grid or random sampling [5, 7].

This thesis contains three works on the application of different techniques to data-driven materials discovery. Becuase machine learning outperforms humans on detailed, tedious, high-dimensional tasks but often struggles with more vague tasks that benefits from additional context or expert input, Chapter 2 investigates how human-artificial-intelligence collaboration can improve the accuracy and interpretability of a machine-learning model for phase classification. Because experimental characterization is often expensive and data-limited, Chapter 3 explores how quantum kernel machine learning can reduce the number of measurements required in an autonomous campaign by learning relationships between X-ray diffraction patterns. Because promising material systems are not known a priori, Chapter 4 investigates the use of high-throughput density functional theory calculations to identify candidate materials for further autonomous exploration. Chapter 5 concludes the thesis with a summary of these results and a discussion of future directions in the broader context of data-driven materials discovery.

The contents of this thesis first appeared across several separate publications, each of which had multiple contributors. The author contributions of each work are listed after the conclusion of the corresponding chapter.

# Chapter 2: Human-In-the-Loop for Bayesian Autonomous Materials Phase Mapping[1]

## 2.1 Abstract

Autonomous experimentation combines machine learning and lab automation to select and perform experiments toward user goals. Accordingly, materials optimization using autonomous experimentation requires fewer experiments and less time than Edisonian studies. Integrating knowledge from theory, simulations, literature, and human intuition into the machine learning model can further increase this advantage. We present a set of methods for integrating human input into an autonomous materials exploration campaign for composition-structure phase mapping. The methods are demonstrated on X-ray diffraction data collected from a thin-film ternary combinatorial library. During the campaign, the user can provide input by indicating potential phase boundaries or phase regions with their uncertainty or indicate regions of interest. The input is then integrated through probabilistic priors, resulting in a probabilistic distribution over potential phase maps given the data, model, and human input. We demonstrate an improvement in phase-mapping performance given appropriate human input.

[1] Adapted from Felix Adams, Austin McDannald, Ichiro Takeuchi, and A. Gilad Kusne. Human-in-the-loop for Bayesian autonomous materials phase mapping. *Matter*, 7(2):697–709, February 2024

## 2.2 Introduction

New materials with improved properties are needed to solve modern engineering challenges, but with each year, discovering such materials becomes more difficult [2]. As researchers exhaust simple-to-make materials, they are driven to investigate materials systems with ever more complex synthesis and processing conditions. However, with each new synthesis or processing parameter, the number of potential materials (and materials experiments) grows exponentially. The Edisonian trial-and-error approach cannot scale appropriately [5]. Several strategies for accelerating materials discovery exist. High-throughput combinatorial synthesis creates hundreds of diverse material samples at once, providing a multiplicative acceleration. High-throughput computational models provide a similar speedup. Both these approaches cannot scale to address the exponentially growing search space.

Machine learning (ML) offers a solution by extrapolating knowledge from past experiments (both in lab and in silico) throughout the vast search space and using the results to identify the next experiments that may accelerate the user toward their goals. Experiment selection is performed using active learning – the ML field of optimal experiment design [6]. By focusing on information-rich experiments, an exponential acceleration in research is achievable [5]. Autonomous experimentation (AE) combines such ML algorithms with automated research equipment to perform experiment design, execution, and analysis in a closed loop.

The successful implementations of AE span diverse areas of materials exploration and optimization. For example, AE has accelerated process optimization for chemical vapor deposition of carbon nanotubes using in situ Raman data [9] and chemical mixture optimization for improved optical thin films [10]. AE has accelerated the process of physics model and

parameter determination through control of neutron scattering measurement experiments of magnetic materials [11]. AE was also demonstrated to accelerate materials discovery, guiding X-ray diffraction measurements to learn the composition-structure-property relationship of phase-change memory materials and identifying a novel material [7]. This AE study has resulted in the first (and, to the best of the knowledge of the authors, the only) discovery of a novel best-in-class solid-state material, specifically a phase-change memory material.

Some of these and other past AE systems combine knowledge from physics theory, computation, and experiments. Prior physics theory was integrated into ML algorithms through diverse methods including constraint programming, probabilistic programming, and probabilistic priors. For example, constraint programming was used to integrate Gibbs phase rule into AE X-ray-diffraction-based phase-mapping systems [7, 12]. Probabilistic programming was used to integrate magnetic theory and neutron scattering theory into an AE neutron-scattering-based system for Néel temperature determination of an antiferromagnetic material [11]. Additionally, Bayesian analysis probabilistic priors have been used to integrate knowledge from previous density functional theory calculations and experiments into a probabilistic model controlling AE phase mapping [7].

However, AE systems have yet to systematically incorporate human expertise into an otherwise autonomous closed loop [5, 13]. While algorithms may outperform humans at fast, detailed, high-dimensional, tedious tasks, human experts win out at hard-to-define tasks that require insight beyond the scope of the given task. By combining human expertise with AE ML, one can potentially overcome the individual weaknesses of man and machine to boost AE performance. Such human-computer interaction falls under "human-in-the-loop", a major subfield of computer science [14] and the human-in-the-loop autonomous system paradigm

[15, 16], which aims to elevate both man and machine. While the human-in-the-loop autonomous system paradigm is newly applied to AE, its past applications span the various fields of robotics include autonomous driving [17], flying [18], and surgery [19], as well as improving overall autonomous system safety [20].

There are added benefits to overcoming the challenge of sustainably achieving human-in-the-loop knowledge integration and user interaction – establishing model interpretability and user trust. To ensure the success of the AE and human expert collaboration, the expert must understand the algorithm's current state to know what input to provide. The expert must also trust that there is value in the interaction. As a result, sustainably convincing the user to provide their input requires tackling the ever-present challenges of ML trustworthiness and interpretability [10], for instance by providing human-interpretable visualization of the algorithm's state before and after human input (as done here). Properly addressing the issues of trustworthiness and interpretability is essential to future adoption of such systems in industry research pipelines.

Previous work utilizing human input in AE and materials informatics focused on the human as a client, with three types of interactions: (1) ML-based experiment recommendations, (2) ML-directed human computations, and (3) human-based algorithm parameter updates. ML-based recommendation engines have guided research into diverse materials including phase-change memory materials [21], high-entropy alloys [22], and photovoltaics [23]. Here, ML selects subsequent experiments, the researcher performs the experiments, and the researcher then updates the ML's database with the collected data. Regarding ML-guided human computation, distributed human computing was used to identify X-ray diffraction peaks associated with single phases [24]. This work used a graphical user interface (GUI) to dis-

play X-ray diffraction data to human clients who then identified the location of peaks. An ML algorithm has also directed human-run optical band-gap calculations for ellipsometry measurements [7]. Toward human-based algorithm parameter updates, human input was used by the first iteration of AE-based carbon nanotube process optimization to regularly update experiment design goals to avoid local optima [9].

For this work, we focus on collaborative interaction between human and ML forming a human-AI team, where both provide knowledge of a similar type. In particular, the ML and human expert combine their analysis of data, predictions (i.e., expectations) of future experiment outputs, and the utility – i.e., the quantified value – that they assign to these experiments. The application is AE-accelerated phase mapping guiding subsequent experiments to maximize knowledge of a composition-structure phase map through optimal selection of materials compositions to be characterized by X-ray diffraction. This challenge was selected because boosting the performance of AE phase mapping has been shown to accelerate materials discovery [7, 25].

We integrate human input through a set of probabilistic priors as well as additive and multiplicative functions to combine ML and human knowledge of (1) data analysis, (2) phase map prediction, i.e., structure data extrapolation (rather than phase analysis of X-ray diffraction data), and (3) optimal experiment design. The human expert interacts with the algorithm through a GUI that visualizes ML phase map analysis, predictions, and the utility of choosing any experiment as the subsequent experiment as defined by the acquisition function (Figure 2.1). The work here is demonstrated through a closed-loop AE simulation. We first present a demonstration and efficacy quantification of human input on autonomous phase mapping, then the phase-mapping model, then finally the methodology for human expertise integration.

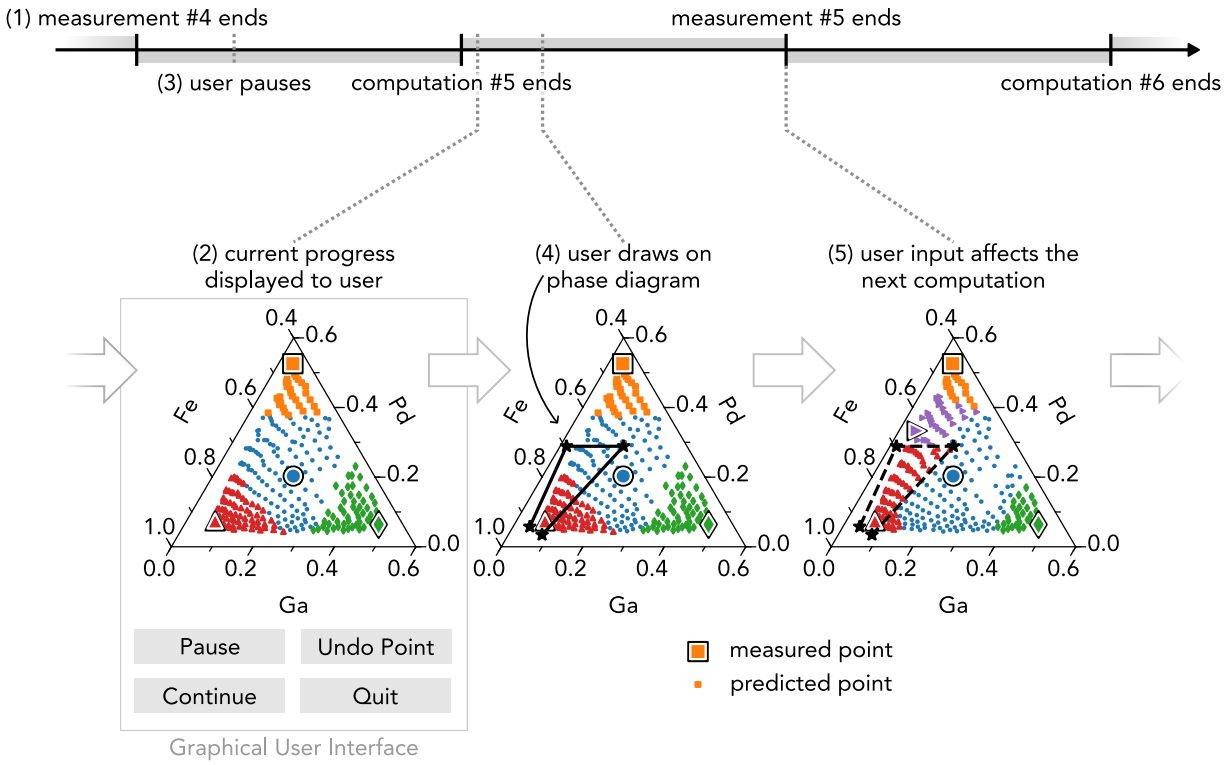



Figure 2.1: User input integration timeline. At the top of the figure is a timeline showing how a computation is performed after every measurement to determine the location of the next measurement. The ternary plots show how the grouping (i.e., clustering) of materials into potential phase regions changes over time. Large, outlined markers indicate measured compositions with known phases, and small markers indicate unmeasured compositions where the model is predicting the phase.

(1) In this example, four compositions have been measured so far.

(2) The model analyzes the collected data, displays the results in a graphical user interface, and begins selecting the fifth composition to be measured.

(3) During this computation, the user indicates their desire to provide input.

(4) During the fifth measurement, the user indicates a phase boundary on the phase diagram.

(5) The user input affects the next computation and the resulting selection of the sixth material to investigate.

## 2.3 Results and Discussion

Figure 2.2 shows how human input for the data analysis stage changes the phase region labels that are assigned to 20 measured compositions compared to a control with no human input. Here, the kernel calculated from the user input is added to the cosine measure similarity matrix used for spectral clustering (with equal weighting), resulting in the change in spectral clustering phase label assignment. Both boundary and region inputs provide the expected changes. The boundary input creates a phase boundary at Pd 35 %. Similarly, the phase region input splits materials identified as belonging to the same phase region (red triangles) into the group found inside the phase region (again, red triangles) and the collection of groups outside the phase region.

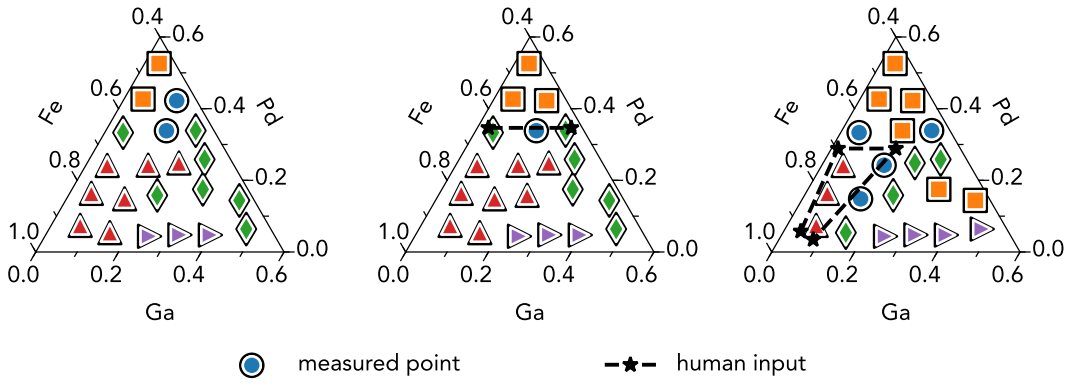
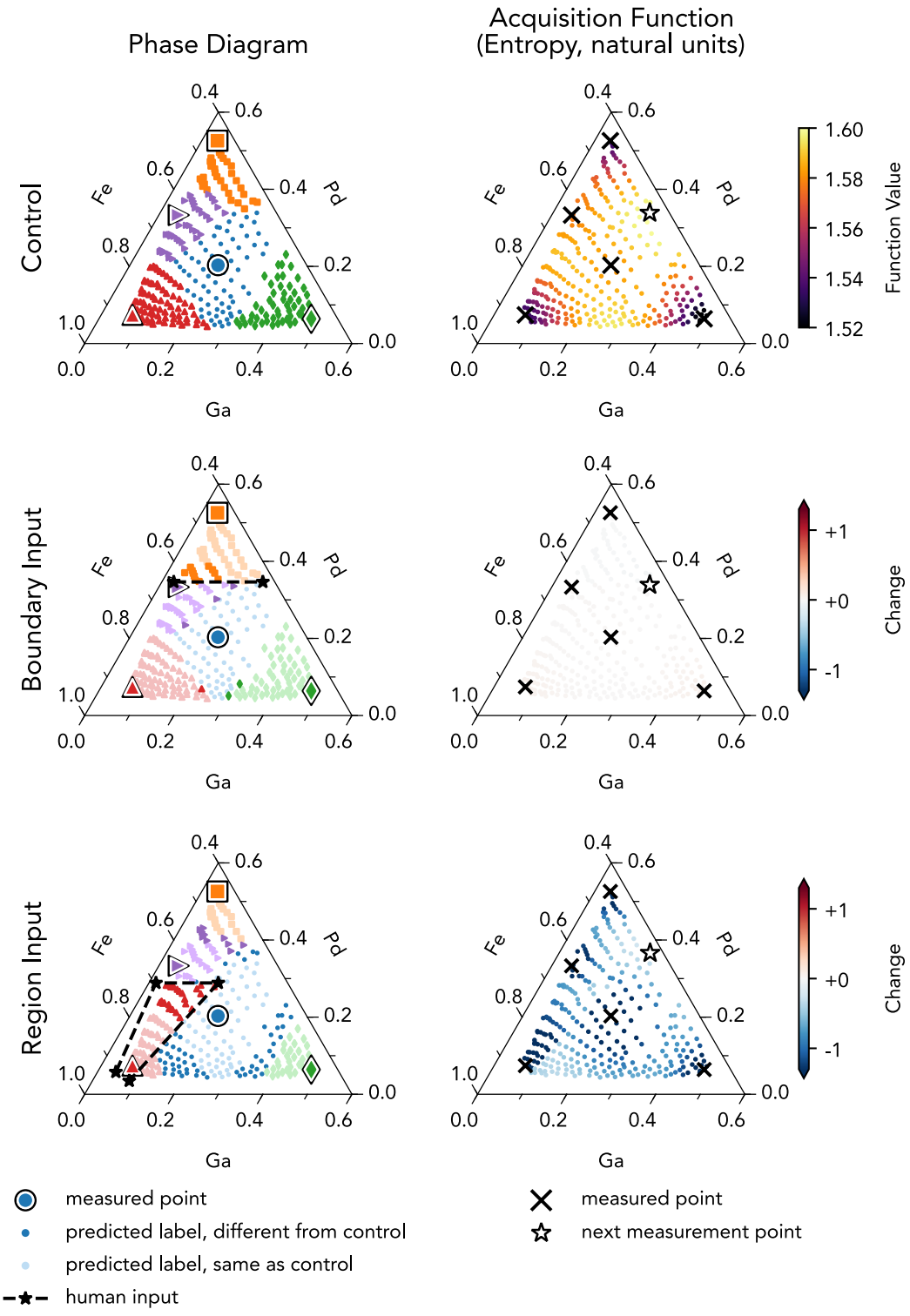



Figure 2.2: The effect of phase boundary human input on phase determination. The ternary plots show the phase labels calculated using spectral clustering on 20 measured compositions. The left plot shows a control with no human input, the center plot shows the effect of a linear phase boundary human input, and the right plot shows the effect of a polygonal phase region human input.

Regarding the prediction stage, the effect of human input depends significantly on the quality of the provided input. The left column of Figure 2.3 shows the model's predicted phase map after five compositions have been measured for either a control or a phase boundary or phase region human input. These are the most likely phase maps given the model, data, and human input. For the control, the algorithm has no human input and no information about the material system between the measured materials, so the phase boundaries are estimated as halfway between measured materials. When the user provides information about phase between measured materials, the local phase boundary aligns with the provided boundary or region. Here, the phase boundary input is close to an existing predicted boundary. As a result, its impacts on phase map prediction and acquisition function values are much smaller than those of the phase region input. The phase region input significantly changes the phase map prediction, which now includes the human-indicated phase region.

In addition to modifying predictions and their accuracy (see discussion of Mann- Whitney U test), human input at the prediction phase modifies the acquisition function used to determine the next measured material. The top right plot of Figure 2.3 shows a heatmap of the entropy acquisition function calculated without human input. The rest of the right column of Figure 2.3 shows the changes in the acquisition function due to human input.

Figure 2.3: The effects of phase boundary human input on ML predictions. The second and third rows of this figure show the effect of a user-provided phase boundary and region compared to a control with no user input shown in the first row. The left column shows the human input with the resulting phase predictions. Large, outlined markers indicate measured compositions with known phases, and small markers indicate unmeasured compositions where the model is predicting the phase. The second column shows the acquisition function values used to choose the next measurement.


Phase Diagram
Acquisition Function
(Entropy, natural units)
Control
Boundary Input
Region Input
Fe
Pd
Ga
0.0
0.2
0.4
0.6
0.8
1.0
Function Value
1.60
1.58
1.56
1.54
1.52
Change
+1
+0
-1
measured point
predicted label, different from control
predicted label, same as control
human input
measured point
next measurement point

For all three test cases, the next materials to investigate (indicated with a star in Figure 2.3, right column plots) are similar. For the control, the acquisition function seeks to improve exploratory knowledge by selecting a material far from the previously collected data, along the edge of the composition space. For the human boundary input, the input boundary falls near an ML-defined boundary (see control) aligning with the same selected material. This increases that material's entropy-measured uncertainty (uncertainty increases along the boundary and decreases near the boundary) and reinforces its selection.

For the region input, phase map knowledge improves in a low-uncertainty area of the composition space. Despite the relative low uncertainty, the phase map is incorrect in this area. As a result, the human provided information that the algorithm may not have sought until later in the research campaign due to this low uncertainty. Thus, prediction accuracy improves while not shifting the selected material. Additionally, entropy is modified locally, with in-region materials dropping in uncertainty and nearby out-of-region materials increasing in relative uncertainty, modifying future material selections. Global uncertainty also reduces. This brings the autonomous system closer to a potential uncertainty threshold – a typical method for ending autonomous exploration.

The results of a Mann-Whitney U test indicate that both inputs significantly affect the accuracy of the ML phase map predictions. Figure 2.4 shows the distribution of the Fowlkes-Mallows Index (FMI), a classification performance metric that varies from 0 (bad) to 1 (good), from 500 trials, and Table 2.1 shows the results of the MannWhitney U test. The Mann-Whitney U test results indicate whether the FMI distribution with human input statistically differs from the distribution without human input. The results suggest that the distributions for both phase boundary inputs are statistically different from the control. However, the lin-

ear boundary had a negative effect on the performance, while the region input had a positive effect. This further suggests that the effect of the human input depends strongly on the quality of the human input.

Human input can also more directly affect the next material investigated. The region of interest input impacts the acquisition function, reducing the utility of materials outside the region of interest while maintaining the relative utility of materials within the region. Figure 2.5 shows how this can be used to limit the domain of the possible future measurements to within a user-defined subspace.

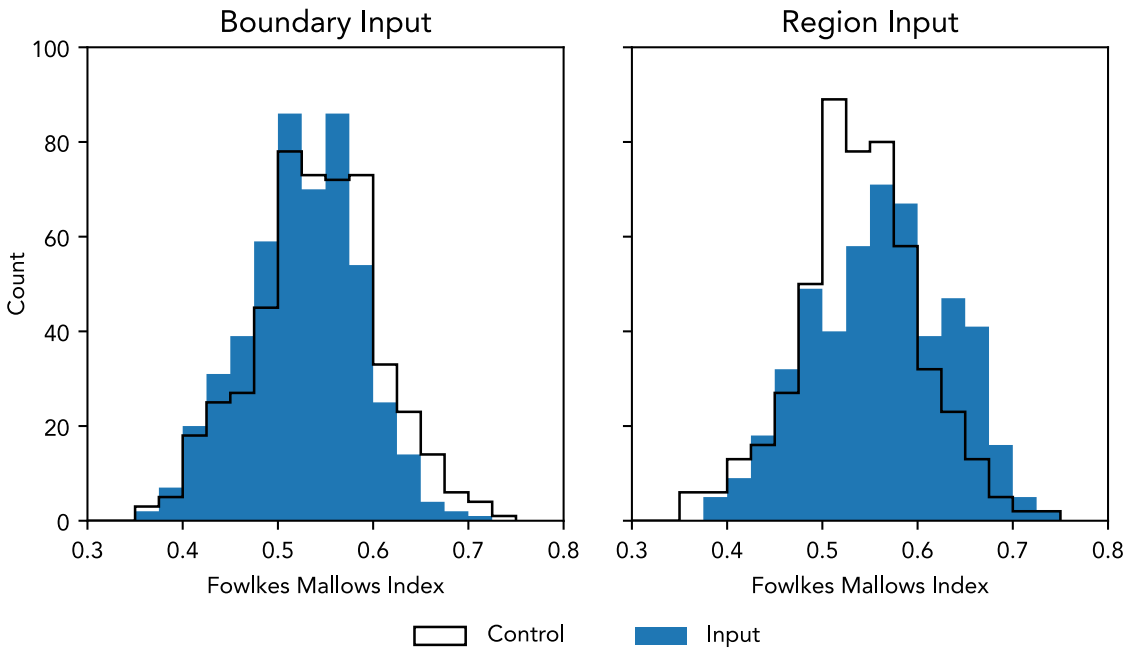



Figure 2.4: Fowlkes-Mallows index results. Histogram of the Fowlkes-Mallows index values used to perform the Mann-Whitney U test for two human input cases: boundary input (left) and region input (right). 500 trials are run for each case with each trial beginning with a random selection of 5 materials.

| | Sample median FMI | Trials | U value | p value |
|---|---|---|---|---|
| Control (no input) | 0.54 | 500 | | |
| Boundary input | 0.53 | 500 | 107,923.5 | $1.8 \times 10^{-4}$ |
| Region input | 0.56 | 500 | 148,534 | $2.6 \times 10^{-7}$ |

Table 2.1: Mann-Whitney U test results. Results of the Mann-Whitney U test performed on the 500 trials for both boundary and region inputs and the resulting Fowlkes-Mallows indices.

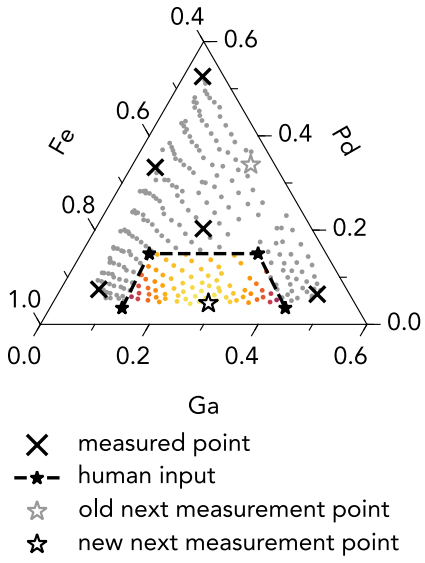



Figure 2.5: The effect of region of interest human input. Compared to the top right plot of Figure 2.2, all the acquisition function values outside of the user-defined region are optionally reduced or neglected. In the latter case, the next measurement point is chosen from inside the region.

## 2.4 Conclusion

We present a technique for human-ML collaboration in the field of autonomous materials phase mapping. Through a GUI and interpretable figures of ML results, the user observes the current state of the AE ML algorithm and can impart their knowledge. Furthermore, we show that by drawing boundaries and regions on ML-computed phase maps, the user can significantly impact data analysis, algorithm prediction, and optimal experiment design.

The example 3-component material system permits the use of 2D GUI visualizations. GUIs and visualizations become more complex for higher numbers of material components (or experiment parameters). One solution is to provide the user with easier-to-understand 2D or 3D "slices" of the target material system. The user provides their input in these slices, and the algorithm then extrapolates the input to the larger space. We believe that such general, interpretable human input methods are essential for the future of autonomous systems in the lab, as they allow experts to work in human-ML teams and establish trust.

## 2.5 Methods

We present a methodology where users can provide input to the AE phase-mapping algorithm to improve phase map data analysis and predictions and to guide selection of subsequent experiments, i.e., experiment design. For this work, we assume that the data analysis stage is performed correctly and is therefore adequate for input to the prediction stage. As a result, it is not included in the human interface workflow presented. Nevertheless, we present results of the equivalent human prior as integrated into the data analysis stage.

For the first workflow task, the algorithm presents the user with the most likely phase map prediction given the data at the current AE iteration, and the user provides their input by drawing phase boundaries or regions on this phase map. To guide selection of subsequent experiments, the algorithm presents the user with its computed utility of potential experiments and the user draws a boundary around their region of interest. Below, we first describe the phase-mapping algorithm and then discuss the methodology for human input integration. The same method was previously used to integrate priors based on computation and exogenous experimental data into phase-mapping predictions [7].

### 2.5.1 Autonomous phase-mapping algorithm

The phase-mapping algorithm is based on the closed-loop autonomous exploration and optimization (CAMEO) algorithm [7], which systematically chooses experiments to learn the composition-structure-property relationship and then exploits that knowledge to find optimal materials. The implementation used here focuses on learning the composition-structure relationship, i.e., the composition phase map. While the more general CAMEO algorithm allows the user to specify an initial guess for the number of phase regions in the phase diagram and then optimizes that number, the algorithm presented holds the number of phase regions at 5 for simplicity of demonstration. For more detailed discussion and justification of the algorithm details including clustering method selection, see Kusne et al. [7].

We use the following notations: $\mathbf{x}_i$ is a vector describing the independent variables of experiment $i$ and $\mathbf{y}_i$ describes the corresponding dependent variable. For the presented case, $\mathbf{x}_i$ is a two-dimensional (2D) vector describing the $i$-th ternary composition and $\mathbf{y}_i$ is the X-ray

diffraction data associated with $\mathbf{x}_i$ . The steps of the phase-mapping algorithm are given by the following.

(1) Data analysis: estimate the phase region membership of measured materials. Spectral clustering is used to group materials which likely belong to the same phase region. $k_{sc}(\mathbf{x}_i, \mathbf{x}_j) = \exp(-d_{i,j}^2)$ is the kernel used to define the similarity between materials generated by experiments $i$ and $j$. Here, $d_{i,j}$ is the cosine metric:

$$d_{i,j} = \frac{\mathbf{y}_i \cdot \mathbf{y}_j}{||\mathbf{y}_i||||\mathbf{y}_j||} \tag{2.1}$$

(2) Prediction, i.e., extrapolation: extrapolate phase region knowledge from X-ray diffraction characterized materials to yet-to-be-measured materials. Here, Gaussian process classification [26] (GPC) is used to extend knowledge of phase region labels from the analysis step across the target composition space, providing a categorical probability of each phase label for each target material. A 2D Matérn 3/2 kernel is used, with a fixed variance of 1 and a fixed length scale of 0.2 elemental fraction. These hyperparameters values were selected and held constant across the presented examples for simplicity of the demonstration, keeping GPC results consistent across AE iterations.

(3) Optimal experiment design: subsequent experiments target materials that maximize knowledge of the phase map. The utility of each experiment toward this goal is computed with the acquisition function ($\alpha$). For this demonstration, experiments are selected that have maximum entropy in the probability distribution across potential phase

region labels:

$$\alpha(\mathbf{x}_i) = \sum_c p_c(\mathbf{x}_i) \ln p_c(\mathbf{x}_i) \tag{2.2}$$

where $p_c$ is the probability that $\mathbf{x}_i$ belongs to phase region $c$. Larger entropy indicates greater uncertainty in phase region label and thus correlates with the position of phase boundaries.

(4) Closing the loop: here, an AE closed-loop system is simulated by identifying the next material to measure from step 3 and then adding the associated premeasured X-ray diffraction pattern to the dataset used by the ML.

### 2.5.2 Human input integration

A user provides input by using a GUI to draw on a phase map. Figure 2.1 shows the timeline for human input integration. In between each measurement, an ML computation is performed to analyze the given data, extrapolate to a predicted phase map, and determine the location of the next measurement. This example spans from the completion of the fourth measurement to the beginning of the sixth. During the fifth computation, the user indicates their desire to provide input using a GUI. While the fifth measurement takes place, the user indicates a cohesive phase segment by drawing a quadrilateral (the central plot). The user can take as long as they need, and their input is used in the next computational stage after they finish. In this example, the user clicks on several points on the phase diagram to define a phase region. Their input affects the sixth computation and the resulting selection of the sixth material to investigate. Incorporating human input incurs a negligible increase in computational cost. The user is not required to provide input every iteration; we expect that the user may pro-

vide input a few times near the beginning of the autonomous campaign when data are sparse and data-only ML prediction capability is low.

We studied user input at all three stages of the autonomous algorithm – data analysis, prediction, and experiment design. For the data analysis stage, the user is shown analysis results and can then indicate a potential phase boundary or phase region. User input at this stage indicates a desire to improve analysis results, which are subsequently used for prediction. For the prediction stage, the user is shown phase map prediction results (as in Figure 2.1) and can then indicate a potential phase boundary or phase region. User input at this stage indicates a desire to modify the predicted phase map. Optimally, the human will provide information different than what would be gained from the next set of measurements, thus adding to overall knowledge. For the experiment design stage, the user is shown a heatmap of the $\alpha$, used to determine the next measurement. They can then provide a region of interest, which will guide the selection of subsequent materials.

The three input types of phase boundary, phase region, and region of interest have differing impacts. The phase boundary input serves to indicate a division between phase regions. The phase region input defines a set of materials as belonging to the same phase region, different from other phase regions. And the region of interest defines a portion of the target material system (e.g., composition space) to investigate. The presented algorithm is human-centric regarding user input. The human provides input based on their desire and intuition, which may not align with algorithm needs such as current prediction uncertainties.

### 2.5.3 Phase region and phase boundary inputs

In the data analysis and prediction stages, human input is integrated by modifying the kernel function used in spectral clustering or GPC, respectively. GPC is a probabilistic classification method: rather than just outputting a classification estimate, it provides a full posterior probability including a prediction of the most likely classification and a quantification of uncertainty. Underlying GPC is the search for a set of latent functions $f_c$, each used to quantify the probability of input $\mathbf{x}_i$ belonging to class $c$. Each latent function is sampled from a multivariate normal distribution $f_c \sim N(\mu_c, K)$, where $\mu_c$ is the distribution mean and $K$ is the covariance kernel matrix. A kernel function $k$ is applied to a finite number of input vector data points to define the kernel matrix: $K_{ij} = k(\mathbf{x}_i, \mathbf{x}_j)$. Together, $\mu_c$ and $K$ define a prior over the form of $f$. Typically, $\mu_c = 0$ due to a lack of prior knowledge of the mean behavior of $f_c$. $K$ is designed to impose probabilistic prior assumptions of $f_c$'s covariance behavior. For instance, if $k$ is selected to be a radial basis function, then $f_c$ must be a smooth function, with a larger kernel length scale resulting in larger contiguous regions of similar class. One can thus design the mean and kernel for off-the-shelf GPC algorithms to integrate human knowledge into the probabilistic prior.

To integrate human input into the kernel, the input is first encoded as a vector, $\mathbf{v}_i$, as described below. The kernel matrix $K_{ij}$ is then updated to $K_{ij} = k(\mathbf{x}_i, \mathbf{x}_j, \mathbf{v}_i, \mathbf{v}_j)$, integrating human input as a probabilistic prior. For example, one can employ the additive kernel $K'_{ij} = \beta_x k_x(\mathbf{x}_i, \mathbf{x}_j) + \beta_v k_v(\mathbf{v}_i, \mathbf{v}_j)$, or the multiplicative kernel $K'_{ij} = k_x(\mathbf{x}_i, \mathbf{x}_j) k_v(\mathbf{v}_i, \mathbf{v}_j)$. The additive kernel mirrors a logical OR statement, where the kernel has a large value if either $k_x$ or $k_v$ has a large value. Additionally, if $\beta_v \gg \beta_x$, the human input prior dominates the prediction.

$\beta_v/\beta_x$ can thus be selected to quantify human certainty in their input. The multiplicative kernel mirrors a logical AND statement, where the kernel has a large value if both $k_x$ and $k_v$ have large values, and vice versa. In this work, we use $\beta_v = \beta_x$, indicating a user with 50 % confidence in their input.

For the phase region input, the user draws a polygon to enclose a segment of the composition space they believe contains materials sharing the same phase region. $\mathbf{v}_i$ is then defined for each material, with one of two (arbitrary but different) values based on whether the material (i.e., experiment) $\mathbf{x}_i$ falls within or without the region. The variable $\mathbf{v}_i$ serves the intermediary step of encoding human input for computing the kernel. The kernel $k_v$ is then defined by

$$k_v(\mathbf{v}_i, \mathbf{v}_j) = \begin{cases} 1 & \mathbf{v}_i = \mathbf{v}_j \\ 0 & \mathbf{v}_i \neq \mathbf{v}_j \end{cases} \tag{2.3}$$

i.e., $k_v = 1$ if the compositions of two materials both fall within or without the region and 0 otherwise. The boundary input is defined similarly for the provided example. Materials $\mathbf{x}_i$ falling on the same side of the boundary are given the same value $\mathbf{v}_i$ and different values otherwise. As a result, we have $k_v = 1$ for a pair of materials on the same side of the boundary and 0 otherwise.

We chose this $k_v$ kernel for its simplicity in adding to or multiplying with $k_x$. To differentiate boundary input from region input more explicitly, one can decrease the value of $k_v$ as a function of distance from the indicated phase region or from the indicated linear phase boundary.

### 2.5.4 Region of interest input

The region of interest input modifies the $\alpha$. The user encloses a portion of the composition space believed to contain materials of high interest with

$$r(\mathbf{x}_i) = \begin{cases} 1 & \mathbf{x}_i \text{ is inside the boundary} \\ \\ 0 & \mathbf{x}_i \text{ is outside the boundary} \end{cases} \tag{2.4}$$

The learned $\alpha$ is then modified by either $\alpha' = \alpha(\mathbf{x})r(\mathbf{x})$ or $\alpha' = \beta_\alpha\alpha(\mathbf{x}) + \beta_r r(\mathbf{x})$, where $\beta_\alpha$ and $\beta_r$ are constants. The former model restricts the subsequent search to within the boundary. The latter model boosts utility values within the region. Additionally, the simpler, former method ensures that the system will always select materials within the user's region of interest. The latter allows the algorithm to overrule the user, based on the $\alpha$. Selection of method depends on the autonomous system's goals or whether the autonomous system should primarily serve the expert's selections or should overrule human-input-based need, defined by the $\alpha$. For this work, we demonstrate the former method.

The selection of $\beta$ coefficients may be defined to normalize the contribution of human input and $\alpha$, ensuring a balanced impact of model output (encoded in $\alpha$) and user input. Additionally, $\beta$ weights are typically scheduled to vary as the gathered data increase. A similar effect can be introduced with the weight $\beta_v$. By reducing $\beta_v$ as the number of local data points increases, one can ensure that any bias introduced by human input will decrease as associated measured data increase.

### 2.5.5 Integrated workflow

The workflow for human input integration at each AE stage (as described in Autonomous phase-mapping algorithm) is as follows.

(1) Data analysis: first, spectral clustering is applied to past collected data to provide phase region labels. The user is then shown a visualization of the computed phase region labels. If the user wishes to provide input, then user phase region or boundary input is integrated through the spectral clustering kernel as described above in the section Phase region and phase boundary inputs, providing a human input prior to the clustering. This results in updated phase region labels for past investigated materials.

(2) Prediction: phase region labels from the data analysis stage are used to compute the GPC phase map prediction – a categorical distribution defining the probability of a phase region label for each target material in the material system. The user is then shown a visualization of the phase map prediction. If the user wishes to provide input, a user phase region or boundary input is integrated through the GPC kernel as described above in the section Phase region and phase boundary inputs, providing a human input prior to the GPC prediction. This results in an updated prediction but does not impact phase region labels assigned during clustering.

(3) Experiment design: the GPC categorical distribution output is used to compute the entropy $\alpha$. The user is shown a visualization of the $\alpha$. If the user wishes to provide input, then the user-defined region of interest impacts the acquisition values as described above in the section Region of interest input. This user input does not impact phase region la-

bels for measured materials or the predicted phase map categorical distribution. Here, human input modifies experiment utility through direct user impact on the $\alpha$ rather than providing a prior that impacts the prediction.

### 2.5.6 Evaluating human-in-the-loop performance

To qualitatively determine how human input affects AE, we performed simulated AE with and without human input using the Fe-Ga-Pd ternary diffraction dataset [27]. We allowed the AE to collect five data points, the human expert then provides their input, and we then investigated the performance of the resulting algorithm phase map predictions by comparing them to the ground truth using the FMI [28]. Here, the ground truth was determined by human expert critical evaluation of the data [27]. We compared three inputs: a linear phase boundary, a polygonal phase boundary, and a region of interest. For the phase boundary input, we used a phase boundary similar to (though not exactly the same as) those present in the true phase map as provided by Long et al. [27] and Kusne et al. [29] (using the same X-ray diffraction 2q range). We analyzed the effect of human input early in the AE so that the model's predicted phase map is rudimentary and does not match the ground truth. Phase map results with all materials measured follow those presented in the supplemental information of Kusne et al. [7].

To quantify the effect of the human input on the accuracy of the phase map predictions (as calculated using the FMI), we performed 500 trials for both phase boundary inputs, calculated the accuracy of the predictions, and compared them to a control using a Mann-Whitney U test. For each trial, the AE algorithm was given five randomly selected compositions and one of the human inputs described above. The resulting phase map predictions were compared to

the ground-truth phase map using FMI [28]. A two-sided Mann-Whitney U test was used to determine if the difference in the FMI due to human input was statistically significant [30]. The Mann-Whitney U test evaluates whether two distributions are statistically different by comparing observation probabilities between two sample populations.

## 2.6 Original Author Contributions

In order of contribution, beginning with largest contribution: **conceptualization**, A.G.K., I.T., F.A., and A.M.; **methodology**, A.G.K., F.A., A.M., and I.T.; **software**, F.A. and A.G.K.; **formal analysis**, F.A.; **investigation**, F.A.; **writing – original draft**, F.A.; **writing – review & editing**, F.A., A.G.K., and I.T.; **visualization**, F.A., I.T., and A.G.K.; **supervision**, A.G.K. and I.T.; and **funding acquisition**, I.T.

# Chapter 3: Quantum Kernel Machine Learning for Autonomous Materials Science[2]

## 3.1 Abstract

Autonomous materials science, where active learning is used to navigate large compositional phase space, has emerged as a powerful vehicle to rapidly explore new materials. A crucial aspect of autonomous materials science is exploring new materials using as little data as possible. Gaussian process-based active learning allows effective charting of multi-dimensional parameter space with a limited number of training data, and thus is a common algorithmic choice for autonomous materials science. An integral part of the autonomous workflow is the application of kernel functions for quantifying similarities among measured data points. A recent theoretical breakthrough has shown that quantum kernel models can achieve similar performance with less training data than classical kernel models. This signals the possible advantage of applying quantum kernel machine learning to autonomous materials discovery. In this work, we compare quantum and classical kernels for their utility in sequential phase space navigation for autonomous materials science. Specifically, we compute a quantum kernel and several classical kernels for x-ray diffraction patterns taken from an Fe-Ga-Pd ternary composition spread library. We conduct our study on both IonQ's Aria trapped ion quantum computer hardware and the corresponding classical noisy simulator. We experimentally verify that a quantum kernel model can outperform some classical kernel models. The results highlight the potential of quantum kernel machine learning methods for acceler-

[2]Adapted from Felix Adams, Daiwei Zhu, David W. Steuerman, A. Gilad Kusne, and Ichiro Takeuchi. Quantum kernel machine learning for autonomous materials science. *APL Quantum*, 3(1):016115, 03 2026

ating materials discovery and suggest complex x-ray diffraction data is a candidate for robust quantum kernel model advantage.

## 3.2 Introduction

Discovery and optimization of new materials play a crucial role in advancing technology in modern society. However, the space of possible compositions and synthesis parameters is immense. Researchers are increasingly relying on high-throughput experimental and computational approaches to identify new functional compounds for their use in a variety of technological areas. Autonomous materials science has emerged as an effective vehicle for navigating the space of possible materials.

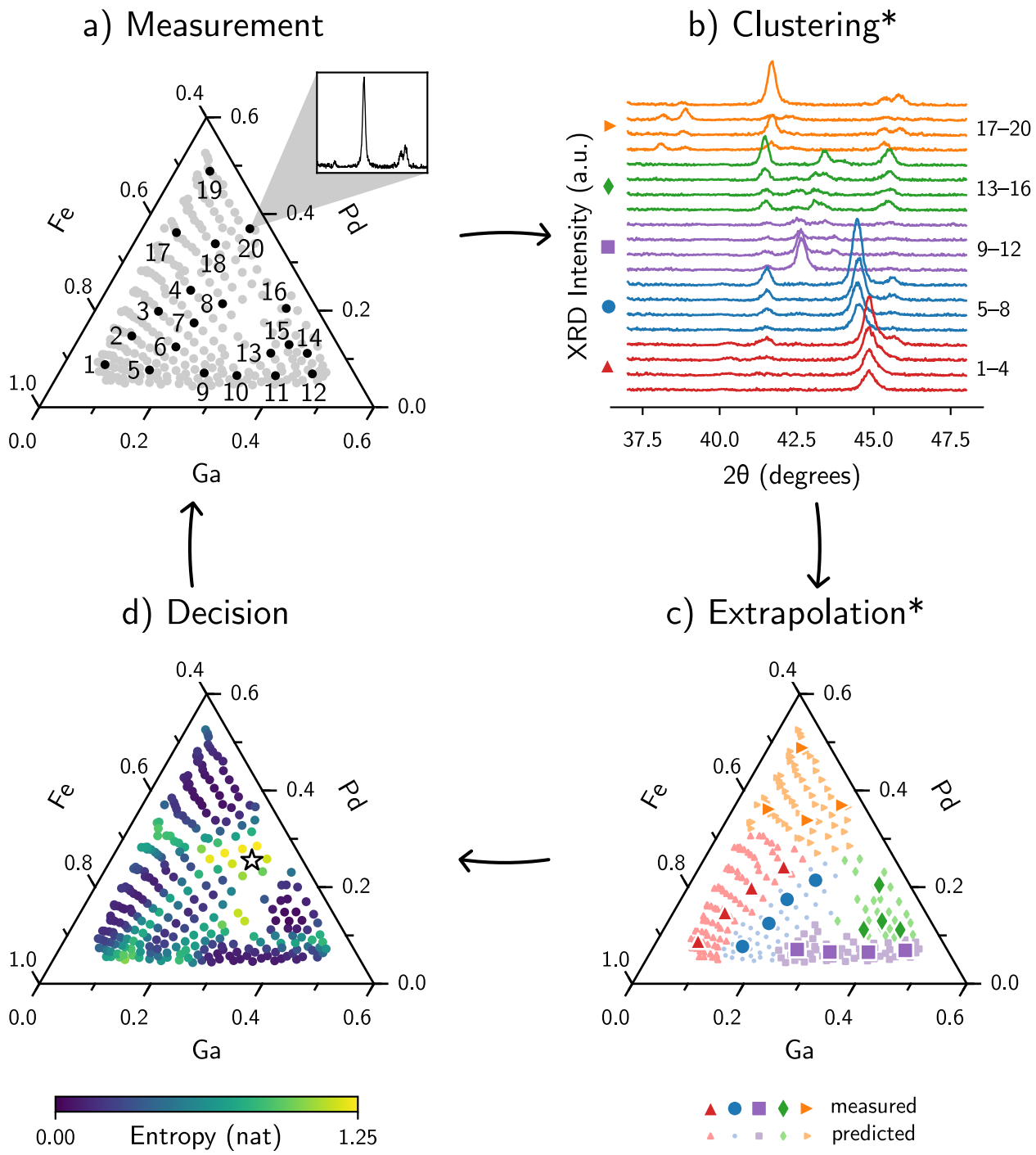
Autonomous experimental methods can self-navigate multi-dimensional parameter space through continuous updating of a Bayesian surrogate model without having to survey every point in the parameter space. There have been a number of demonstrations of closed-loop autonomous workflows for successful optimization of compositional parameters (with respect to specific materials characteristics) with only a limited number of experimental iterations in self-guided sequences [5, 7, 32–34].

Combinatorial libraries, where large compositional variations are laid out on individual wafers/chips, are particularly useful physical platforms for materials optimization. Autonomous optimization within libraries can be used to quickly chart materials within fixed composition variations such as ternary phase diagrams [35].

Figure 3.1 shows a schematic of an example typical active learning workflow as applied to the Fe-Ga-Pd ternary composition space. The goal of the autonomous workflow is to determine

the distribution of the different crystalline phases throughout the composition space ("phase map"), obtained using XRD measurements, using as few measurements as possible. The iterative workflow has 4 steps: measurement, clustering, extrapolation, and decision. First, an XRD measurement is performed at a particular composition. Second, all the XRD patterns measured so far are clustered into groups (representing different crystal phases). Third, the clusters are then extrapolated to the unmeasured compositions. Fourth, the predictions and their uncertainties are used to determine which composition should be measured next. To minimize the total uncertainty in the predicted phase map, the composition with the largest uncertainty is chosen at each iteration. Once the total uncertainty falls below a threshold, we have a reasonable prediction of the phase map of the entire composition space after only measuring a fraction of the composition space.

Figure 3.1: A schematic of a typical iterative autonomous phase mapping workflow. Asterisks (*) indicate which steps use kernel methods. **(a)** A new x-ray diffraction measurement is performed at a specific composition (shown in units of atomic fraction). Sample indices 1 – 20 were chosen manually here for illustration and do not reflect a typical measurement order. **(b)** All of the measured compositions are clustered into groups and assigned a corresponding label (color and symbol to the left) using an *x-ray diffraction* kernel function. **(c)** The labels of the unmeasured compositions are then extrapolated using a *composition* kernel function. **(d)** To minimize the total uncertainty in the extrapolated labels, the composition with the maximum uncertainty (entropy) in its predicted label is chosen as the next composition to measure, indicated by the star. **Note** that the clustering and extrapolation methods are both kernel methods but use different kernel functions which compare different types of data (x-ray diffraction patterns and compositions).


a) Measurement
b) Clustering*
c) Extrapolation*
d) Decision
Fe
Pd
Ga
0.0
0.2
0.4
0.6
0.8
1.0
1
2
3
4
5
6
7
8
9
10
11
12
13
14
15
16
17
18
19
20
XRD Intensity (a.u.)
2θ (degrees)
37.5
40.0
42.5
45.0
47.5
17–20
13–16
9–12
5–8
1–4
measured
predicted
0.00
Entropy (nat)
1.25

Autonomous experiments require a machine learning surrogate model for the property of interest. Popular methods such as deep learning require lots of training data, which aren't available for novel materials. The machine learning subfield of Few-Shot Learning (FSL) studies methods for such data-limited regimes [36]. Experimental materials science data are expensive and therefore limited in general, making some FSL techniques such as transfer learning (where knowledge from one data-rich task is transferred to another data-limited task) challenging [36].

Gaussian processes are a kernel machine learning method commonly used for the extrapolation step of the autonomous materials science workflow. Gaussian processes are an extension of Gaussian distributions: a Gaussian distribution describes the probability distribution of a random value, while a Gaussian process describes the probability distribution of a function [26]. A multivariate Gaussian distribution has a covariance matrix describing the relations between variables, and a Gaussian process has a covariance function describing the relations between function values. This covariance function is the kernel function of the Gaussian process. For more information on Gaussian processes and Gaussian process classification, see reference [26]. We used Gaussian process classification as implemented in GPflow [37].

Quantum kernel machine learning is an emerging area of research that may enable certain functions to be learned with less training data than classical kernel methods, making it a promising tool for autonomous materials discovery. Recent work by Huang et al. demonstrated that classical kernel models can predict the output of quantum kernel models if they are given sufficient training data [38]. However, we are especially interested in the data-limited regime where classical kernel models don't have enough data to outperform quantum kernel models, such as in the first few iterations of the autonomous materials science workflow. As

highlighted by the well-known "No Free Lunch" Theorems [39], the performance of a machine learning model fundamentally depends on the specific problem it is applied to. Therefore, the value of quantum kernel methods hinges on identifying problem domains where they offer a genuine advantage.

Diffraction data might be such a domain where quantum kernel methods have an advantage. Scattering and diffraction (using X-ray, electrons, and neutrons) are ubiquitous characterization tools in materials science as they provide reciprocal representations of periodic atomic positions as well as their electronic and magnetic structures [40]. Diffraction data might provide a data platform on which quantum kernel models can learn faster than classical kernel models because the techniques used to represent diffraction (matrix inversion and the Fourier transform) are thought to be faster on quantum computers. The transformation from real space to reciprocal space can be written as a matrix inversion [40], which is an application where quantum computers have an exponential advantage using the Harrow Hassidim Lloyd (HHL) algorithm [41]. While we don't use either the HHL algorithm or the quantum Fourier transform in this work, the centrality of those problems to analysis of diffraction data suggests that diffraction datasets are a fruitful area to explore for a quantum kernel model advantage.

In this work, we evaluate how well a quantum kernel model can learn an x-ray diffraction (XRD) dataset using IonQ's Aria trapped ion quantum computer. We introduce the XRD dataset and a corresponding typical autonomous materials science workflow, describe the classical and quantum kernels used, explain how we compared the kernels, show the results of the comparison, and discuss their implications. Lourenço et al. recently performed similar work with other, non diffraction materials science datasets: perovskite properties and doped nanoparticle relaxation [42].

This work presents a novel application of quantum kernel machine learning and demonstrates how recent developments in our theoretical understanding of quantum advantage in machine learning can be fruitfully applied to address scientific and engineering challenges.

## 3.3 Methods

### 3.3.1 XRD Dataset

Our experimental materials science dataset is from a ternary Fe-Ga-Pd thin film composition spread which was fabricated by co-sputtering Fe, $Fe_2Ga_3$, and Pd on a 3 inch (7.62 cm) Si wafer such that a continuous variation in composition is created on the wafer [27]. Such composition-spread combinatorial libraries provide a useful platform for exploring new materials within a large ternary compositional phase diagram. The dataset consists of stoichiometric composition information, i.e. $a$, $b$, and $c$ in $Fe_aGa_bPd_c$ (where $a + b + c = 1$), and XRD diffraction patterns taken at 237 uniformly distributed positions/compositions on the library.

XRD of the films was performed using the $\omega$-scan mode of a D8 DISCOVER for combinatorial screening (Bruker-AXS) using an x-ray beam spot size of 1 mm diameter. It is equipped with a GADD two-dimensional detector which captures data for a fixed range of $2\theta$ and $\omega$ at once. The raw detector images are then integrated to obtain the $2\theta$ angles and peak intensities using the D8 GADDS program and a script to automate the process. For more details on the synthesis and XRD characterization processes, see references [27] and [43].

We've used this dataset as a benchmark for other machine learning studies (such as in reference [29]), so the quantum kernel model's performance on this dataset is likely representative of its performance on other materials science datasets.

We sampled this dataset to simulate the first few measurements made in the autonomous materials science workflow. We used 4 XRD patterns from each of the 5 distinct structural phase regions on the wafer for a total of 20 data points. The ground truth phase labels come from human expert analysis of the XRD data [27].

### 3.3.2 Classical and Quantum Kernels for Autonomous Materials Science

Kernel machine learning methods find patterns in data using a kernel function, $k(x_1, x_2)$, which takes two data points $x_1$ and $x_2$ as inputs and returns a value describing how similar the two data points are [44]. We compared the quantum kernel to two classical kernels, a radial basis function ($k_{\text{RBF}}$) and the cosine similarity ($k_{\text{CS}}$):

$$k_{\text{RBF}}(x_1, x_2) = \exp\left(-\frac{||\hat{x}_1 - \hat{x}_2||^2}{2}\right) \tag{3.1}$$

$$k_{\text{CS}}(x_1, x_2) = \hat{x}_1 \cdot \hat{x}_2 \tag{3.2}$$

...where $\cdot$ is the dot product, $||\ ||$ is the Euclidean $L^2$ norm, and $\hat{x}_i$ is the $L^2$ normalized data vector $x_i$. In this work, each $x_i$ is a vector containing the XRD intensity values of an XRD pattern.

The two classical kernels presented for comparison were chosen to illustrate the nature of the potential quantum kernel advantage. The squared exponential $L^2$ norm radial basis function kernel is a common kernel for Gaussian processes, capable of describing arbitrary functions which are sufficiently smooth [26]. The cosine similarity is a simpler similarity measure which works well for clustering XRD patterns using other machine learning methods compared to more sophisticated kernels such as dynamic time warping or earth mover's dis-

tance [45], but is atypical as a Gaussian process kernel because of its simplicity. The polynomial kernel is common in the machine learning literature for high-dimensional classification [26], but is less common for analysis of XRD patterns.

These kernels typically have hyperparameters which are fitted to the data during model training. In this work, to simplify analysis and comparison across different training datasets and dataset sizes, we use fixed hyperparameters which worked well for this dataset.

To calculate a kernel function, $k_Q$, using a quantum computer, we use a feature map quantum circuit, $U$, which receives the values of a data point $x \in \mathbb{R}^d$ ($d$ is the number of data dimensions) as parameters and calculate...

$$k_Q(x_1, x_2) = |\langle 0| U^\dagger(x_2)U(x_1) |0\rangle|^2 \tag{3.3}$$

...i.e., starting with a set of qubits in the state $|0\rangle$, one applies the feature map circuit with the data point $x_1$, applies the conjugate transpose (i.e, the inverse, because the evolution of a closed quantum system is a unitary transformation [46]) of the feature map circuit with the data point $x_2$, then finds the probability that the final state of all the qubits remains $|0\rangle$ [47]. If $x_1$ and $x_2$ are similar, the two feature map circuits mostly cancel out, the probability that the circuit output remains $|0\rangle$ is large, and the kernel value is high. Otherwise, the two feature maps don't cancel out, the circuit outputs an arbitrary state with low probability of being $|0\rangle$, and the kernel value is low. To estimate $k_Q(x_1, x_2)$, the circuit calculation is repeated 1,024 times to determine the approximate probability of measuring $|0\rangle$. This calculation is repeated for every pair of data points to construct a kernel matrix, $K_{i,j} = k(x_i, x_j)$, which is then used by the classical kernel machine learning method.

We used a feature map quantum kernel circuit based on the work of Peters et al. [48] to compare XRD patterns. The quantum feature map circuit is shown in Figure 3.2. The circuit is composed of quantum operations, or "gates", which affect 1 or 2 qubits at a time. The gray, 1-qubit gates are Hadamard gates and the gray 2-qubit gates are $\sqrt{i\text{SWAP}}$ gates. The white, 1-qubit gates are rotation gates, which accept a parameter that determines the angle of rotation. Each group of three rotations (around the $z$, $y$, and $z$ axes again respectively), can describe an arbitrary rotation of the qubit Bloch sphere. The XRD intensities are used as the angle parameters of the rotation gates, after being re-normalized and scaled between $[0, \pi]$ radians. The numbering of the rotation gates indicates the order in which the XRD intensities were used. We used 25 qubits and 6 rotation gates per qubit, totaling 150 XRD intensities (from 150 evenly spaced $2\theta$ values) used in the feature map circuit (the dimension of the input data vector $x_i$). In this work, we used the IonQ Aria trapped ion quantum computer for the quantum circuit execution. Quantum circuits corresponding to kernel function evaluations comparing any element to itself were not performed, instead assuming the ideal value of 1. The classical simulations of the quantum kernel output were performed using IonQ API with the standard Aria noise model.

Eq. 3.3 defines not a single quantum kernel, but a family of kernels parametrized by the choice of feature map circuit $U$. In principle, $U$ can be tailored to known structure in the data, such as permutation-equivariant circuits for graph learning tasks [49] or quantum convolutional architectures for translationally symmetric data [50]. In our XRD classification problem, however, the absolute positions and relative intensities of diffraction peaks are physically meaningful, so neither global permutations nor rigid translations of the 150 intensity values preserve the labels. As a first step, we therefore focus on a single, hardware-efficient

feature map based on Peters et al. [48] that serves as a generic but expressive ansatz compatible with the IonQ Aria device.

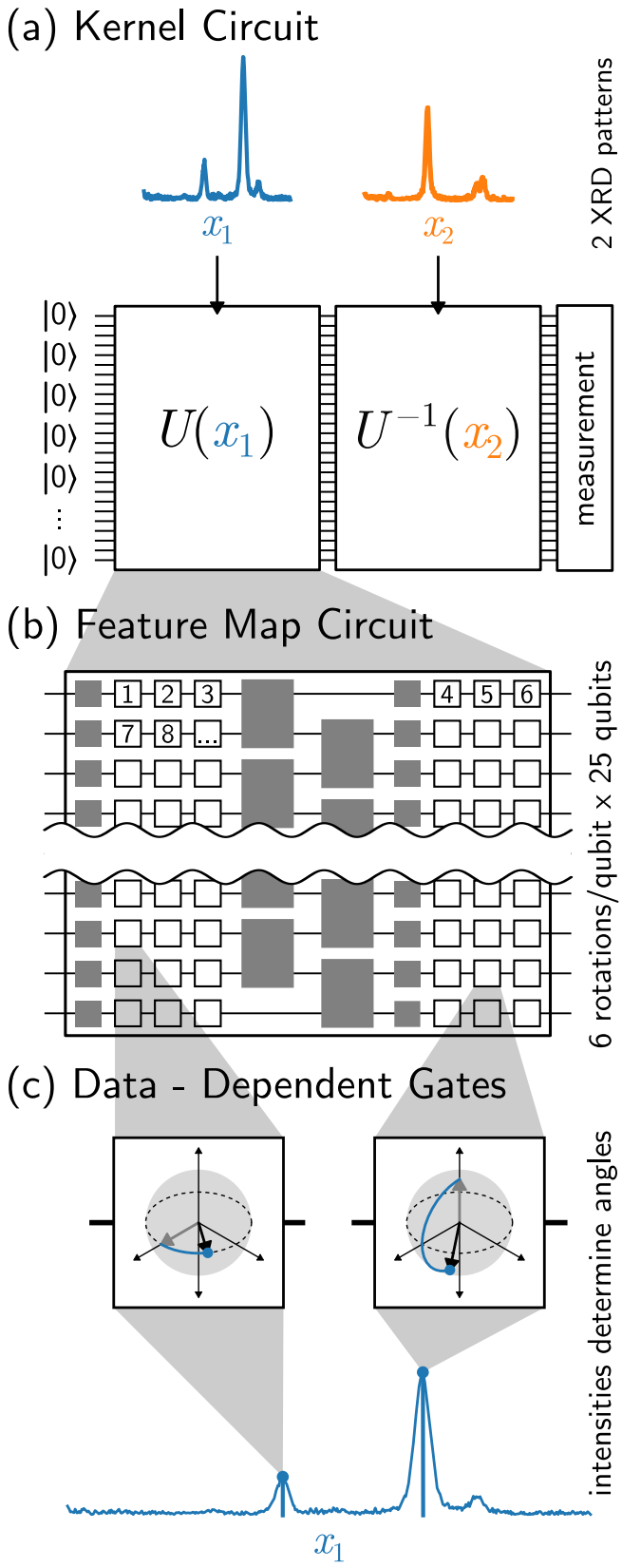
Quantum algorithms for accelerating kernel machine learning calculations have been developed [51], but require the use of Quantum Random Access Memory [44], which is beyond current quantum computers. In this work we used quantum computers to calculate kernel functions which are then used by classical machine learning methods [47,52], as this approach is feasible with current technology.

### 3.3.3 Evaluating Quantum Kernel Performance

To determine a quantum kernel's theoretical potential for quantum advantage, one can use the quantities defined by Huang et al. [38]: the model complexities of the quantum and classical kernels and the geometric difference between the kernels. The model complexity $s$ for kernel matrix $K$ is defined as...

$$s_K(N) = \sum_{i,j=1}^{N} (K^{-1})_{i,j}(2y_i \cdot y_j - 1) \tag{3.4}$$

Figure 3.2: The quantum circuit used to compare two XRD patterns, $x_1$ and $x_2$. **(a)** The kernel circuit is composed of a forward and a reverse copy of the feature map circuit, $U$, which takes the intensities of an XRD pattern as parameters. The initial state of each qubit is $|0\rangle$ and the kernel value is the probability that the final state of every qubit is $|0\rangle$. **(b)** The feature map circuit, $U$, is composed of 1- and 2-qubit operations, or "gates". Each horizontal line represents a qubit, and the circuit computation proceeds from left to right. The gray, 1-qubit gate is a Hadamard gate, the gray 2-qubit gate is a $\sqrt{i\text{SWAP}}$ gate, and the triplets of white gates are rotation gates about the $z$, $y$, and $z$ axes respectively. The numbers indicate the order in which XRD intensities parameterize the rotation gates. **(c)** A schematic illustrating how the XRD intensities determine the angle of rotation in the rotation gates, a $z$ axis rotation on the left and a $y$ axis rotation on the right.


(a) Kernel Circuit
2 XRD patterns
$x_1$
$x_2$
$|0\rangle$
$|0\rangle$
$|0\rangle$
$|0\rangle$
$|0\rangle$
$|0\rangle$
$U(x_1)$
$U^{-1}(x_2)$
measurement
(b) Feature Map Circuit
1
2
3
4
5
6
7
8
...
6 rotations/qubit × 25 qubits
(c) Data - Dependent Gates
intensities determine angles
$x_1$

...where $K^{-1}$ is the inverse of the kernel matrix, $N$ is the number of data points, and $y_i$ and $y_j$ are the one-hot encodings of the phase labels of each composition (such that $(2y_i \cdot y_j - 1)$ equals 1 if the labels are the same, otherwise $-1$). The geometric difference between the classical and quantum kernel, $g_{CQ}$, is defined as...

$$g_{CQ} = \sqrt{\|\sqrt{K_Q}(K_C)^{-1}\sqrt{K_Q}\|_\infty} \tag{3.5}$$

...where $K_C$ is the classical kernel matrix, $K_Q$ is the quantum kernel matrix, and $\| \ \|_\infty$ is the spectral norm [38]. The matrix square roots and inverses can be efficiently computed using the singular value decomposition. See the Supplemental Information (SI) for more details.

The model complexity is used to define an upper bound on the model's expected error as a function of the number of training data points. For a model $h(x)$ trying to predict some true labels $f(x)$, the expected value of the absolute difference between the model predictions and the true labels over the input domain $\mathbb{D}$ is...

$$E_{x\in\mathbb{D}}(|h(x) - f(x)|) \leq c\sqrt{\frac{s_K(N)}{N}} \tag{3.6}$$

...for some constant $c > 0$ [38]. This upper bound on the expected error decreases as more data is collected and increases with increasing model complexity, so the model complexity should be as small as possible to reduce the expected error. If the classical model complexity is much higher than the quantum model complexity, then the quantum model might have lower expected error when $N$ is small (i.e., when there is very little training data).

The geometric difference is used to define another upper bound, this time on the clas-

sical model complexity. The geometric difference and model complexities obey the following relation:

$$s_C \leq g_{CQ}^2 s_Q \tag{3.7}$$

...where $s_C$ and $s_Q$ are the classical kernel and quantum kernel model complexities, respectively [38]. In order for the classical model complexity to be much higher than the quantum model complexity, the geometric difference must be large.

First, to predict whether a quantum kernel might have an advantage over classical kernels for any dataset, one uses the geometric difference. If the geometric difference is small, no advantage exists for that quantum kernel because the largest classical model complexity will be close to the quantum model complexity, regardless of dataset [38]. However, if the geometric difference is large, there exists a dataset for which the classical model complexity (and thus the upper bound on the expected error) is much higher than the quantum model [38].

Second, to predict whether a quantum kernel might have an advantage over classical kernels for a specific dataset, one uses the model complexities. If the model complexities are similar, the expected error upper bounds are also similar, and the classical model can learn the dataset as easily as the quantum model [38]. However, if the classical model complexity is much higher than the quantum model complexity, then the upper bound on the expected error of the classical model is also much higher, and it's possible that the quantum model learns the dataset faster than the classical model [38].

In addition to Huang et al.'s analysis [38], we empirically tested the quantum kernel on a supervised learning task adjacent to the typical autonomous workflow described above. In the above workflow, an XRD kernel function is used for the unsupervised task of clustering the

XRD patterns into groups, while Huang et al.'s analysis applies to the supervised learning task of assigning labels to new data based on labeled training data. The supervised extrapolation step of the above workflow uses a composition kernel function, not an XRD kernel function. So, instead of using the quantum kernel for clustering XRD patterns, as in the above workflow, we studied a supervised learning task similar to tasks in the autonomous workflow: we trained a Gaussian process model to extrapolate the phase labels from human-expert-labeled XRD patterns to unlabeled XRD patterns. This task is a useful proxy for understanding the utility of the quantum kernels for autonomous materials science because we expect that a model which requires less training data to achieve a certain accuracy threshold for this task would also require less training data to achieve a certain uncertainty threshold in an active learning setting.

To evaluate the performance of the kernels, we measured the subset accuracy of the Gaussian process classifier as a function of the number of training data points. For each training set size, $N$, we chose 20 subsets of size $N$ from the 20 experimental XRD data points for training. The subsets were chosen uniformly at random without regard for the true labels (except for $N = 19$ training data points, where we used all 20 subsets of size 19). We then calculated the number of correct test labels for each training set. In the parlance of FSL, we evaluated each kernel's 5 way $n$ shot accuracy, for $n = 1$ to 4 depending on the training set size and random samples. We then compared the relative accuracy of the quantum and classical kernels, expressed as the ratio of their accuracies. This is analogous to relative risk, for which confidence intervals can be computed using the Katz method (Method C in ref. [53]) as implemented in SciPy, wherein the log of the ratio is taken to be normally distributed.

## 3.4 Results and Discussion

### 3.4.1 Kernel Matrix Values

The quantum kernel matrix displays relationships between XRD patterns which weren't found by either of the classical kernels. Figure 3.3 shows the kernel matrices for all 20 XRD patterns. Figure 3.3 (a) and (b) show the quantum kernel matrices as simulated on a classical computer and measured on the IonQ Aria trapped ion quantum computer, respectively. Figure 3.3 (c) and (d) show the classical kernel matrices used for comparison. All the kernel matrices show that XRD patterns 1–4 and 5–8 form distinct groups which are more similar to each other than to other patterns and that patterns 9–12, 13–16, and 17–20 also form groups of 4 but are more interrelated. The quantum kernel found some faint inter-group similarities that weren't found by the classical kernels: patterns 1, 2, 5, and 6 are similar to several patterns outside their groups of 4. The quantum kernels are shown with a logarithmic scale to show these faint relationships, while the classical kernels are shown with a linear scale because they don't have any small values $< 0.1$. For comparison, all kernels in both linear and log scales are available in the SI.

The relationships found by the quantum kernel and missed by the classical kernels are between XRD patterns with generally low intensity. Refer to Figure 3.1 (b) to see the XRD patterns. Groups 1–4 and 5–8 both correspond to a body centered cubic Fe phase, but with significant peak shifting due to composition-dependent crystal lattice parameter changes [54]. However, in XRD patterns 1, 2, 5, and 6, the largest peak has a lower maximum intensity compared to other patterns in their groups. Similarly, XRD patterns 11–15 and 17–19 have no

large peaks.

These relationships between low intensity XRD patterns were missed by the classical kernels because they are magnitude-invariant, while the quantum kernel is magnitude-dependent. The classical kernels we used for comparison are defined in terms of normalized vectors, so they can't compare relative XRD intensities. The same is true for typical (but not all) XRD similarity measures, such as the Pearson's correlation coefficient. The output of the feature map circuit, however, does depend on the magnitude of the input data point, so the quantum kernel can compare the relative intensities of two XRD patterns. As a result, the quantum kernel identifies XRD patterns with generally low intensity as similar.

The kernel values as measured on the quantum computer are similar to the simulated values, except for a systematic decrease in kernel values due to additional hardware noise. As the calculation proceeds, errors accumulate and the two copies of the feature map circuit are less likely to cancel out, leading to decreased kernel values. Some of the fine details in the measured quantum kernel are sufficiently reduced that they are no longer detected because of the finite sampling used to calculate the kernel values.

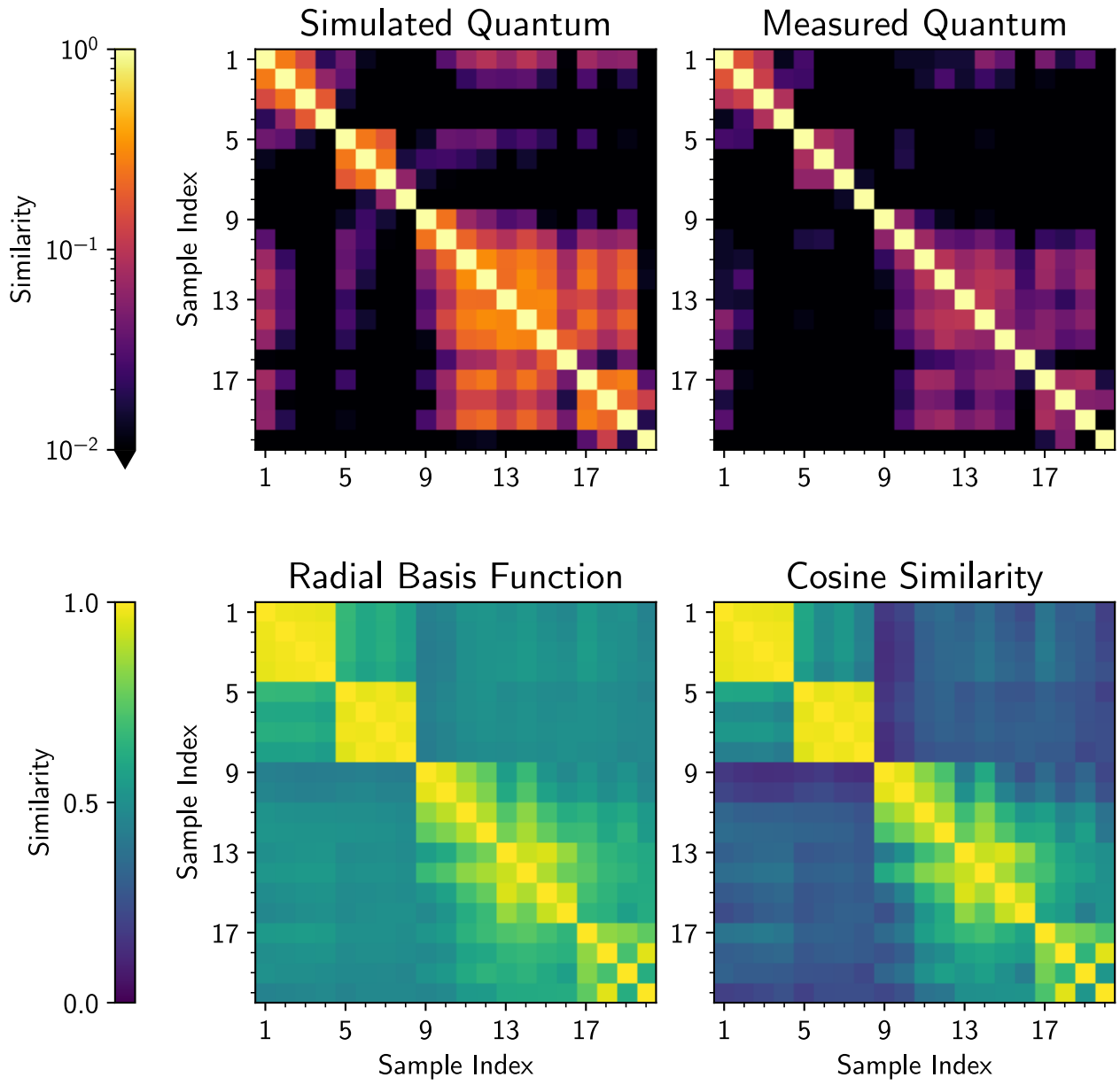



Figure 3.3: Comparison of the quantum and classical kernel matrices. The axis values are sample indices from Figure 3.1a. Quantum kernel matrices are shown with a logarithmic colormap to show the fine details not picked up by the classical kernels, while the classical kernels are shown with a linear colormap. See SI for all kernels in both logarithmic and linear scales.

### 3.4.2 Model Complexities and Performance

| Kernel | Geometric Difference | Model Complexity |
|---|---|---|
| Simulated Quantum | 10.74 | 19.44 |
| Measured Quantum | 10.92 | 20.27 |
| Cosine Similarity | | 36.85 |
| Radial Basis Function | | 37.20 |

Table 3.1: The results of the geometric difference and model complexity analyses. We calculated the geometric difference values with respect to both the classical kernels and show the worst case results (the Radial Basis Function kernel).

The geometric difference and model complexity calculations, shown in Table 3.1, suggest that the quantum kernel model could require less training data than the classical kernel models on the XRD dataset. The geometric difference between the classical and quantum kernels is greater than $\approx \sqrt{N}$, which indicates that there exists a dataset for which the classical model complexity is higher than the quantum model complexity. Indeed, the classical model complexity for our XRD dataset is higher than the quantum model complexity, which means that the upper bound on the expected error is higher for the classical kernel model. The analysis therefore suggests that it is possible that the quantum kernel model could have better performance with limited training data.

Figure 3.4 shows the performance of the Gaussian process model using the quantum kernel relative to the classical kernels as a function of the training set size. See the SI for separate kernel accuracies. The shaded regions indicate 95 % confidence intervals. The confidence intervals expand as the number of training data points increase because there are fewer testing data points (out of the total 20 data points) with which to evaluate the model performance, decreasing the sample size. Comparing the performance of the simulated and measured quan-

tum kernel models, the performance of the measured quantum kernel model is slightly lower for some training set sizes, indicating that reducing hardware noise could improve the performance of the quantum kernel model.

The empirical results show that the quantum kernel model requires less training data than only one of the two classical kernel models within a certain range of training set sizes. Between about 10 and 15 training data points, the quantum kernel model outperforms the radial basis function classical kernel model, until about 15 and 19 training data points, where the classical kernel has enough data to achieve similar performance. With less than 10 training data points, neither the quantum nor radial basis function kernel has much data, and the radial basis function kernel happens to perform better. The cosine similarity, despite having a kernel

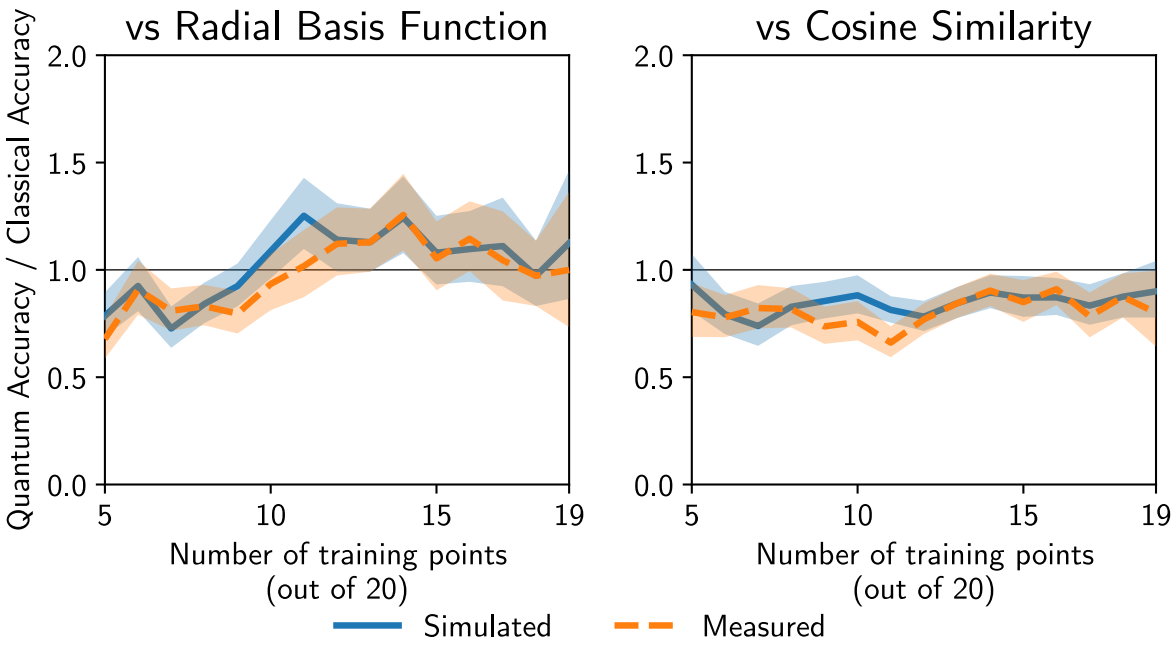



Figure 3.4: The relative performance of the quantum and classical kernels on the supervised learning task. Both plots show the accuracy of the Gaussian process classifier using the quantum kernel (simulated and measured) relative to one of the classical kernels. The left plot is relative to the radial basis function kernel and the right plot is relative to the cosine similarity kernel. The shaded regions indicate 95 % confidence intervals.

matrix not unlike the radial basis function kernel, outperforms all other kernels for this dataset.

The model complexity and performance depend on the combination of dataset and kernel function. For example, the quantum model complexity is less than the classical model complexities, even though the quantum kernel matrix captured more nuanced relationships in the data because of its magnitude dependence. Also, the cosine similarity outperformed all other methods for this dataset despite its magnitude invariance.

To further illustrate how sensitive the performance of the models is to their suitability for a particular problem, we compared the performance of the quantum kernel and cosine similarity on arbitrary, engineered labels constructed to minimize the performance of the cosine similarity. The results of this comparison are shown in Figure 3.5. Drawing on the work of Huang et al. [38] again, these binary labels are constructed to maximize the model complexity of the cosine similarity kernel model. For details on the constructions of these labels, see the SI. With these labels, the cosine similarity, which previously outperformed all other models, does much worse than the quantum kernel. See the SI for the accuracy on the engineered data for each kernel separately.

These results, and the work of Huang et al. [38], can be understood in terms of model bias and its relationship to model complexity. In this context, the bias of a model is the difference between the expected value of the model's prediction and the true value it's trying to predict [55]. As the complexity of a model increases, it can make more nuanced predictions, and thus its bias decreases [56]. However, as Huang et al. showed, increasing the model complexity also increases the amount of data required to train the model [38]. The data-limited regimes of materials science thus reward simple, low-complexity models. Simple models, however, are necessarily inflexible and must be carefully chosen to match the problem at hand.

With this understanding, our results suggest that quantum kernel machine learning models can outperform classical kernel models, but the quantum kernel needs to have an appropriate inductive bias. The inductive bias of a machine learning model is the set of assumptions that the model uses to make predictions [55]. The quantum kernel outperforms the radial basis function kernel once enough data is collected because it has lower model complexity and thus requires less training data. However, the cosine kernel outperforms both other kernels because its inductive bias is a better fit for this classification task. This indicates that a quantum kernel with low model complexity and appropriate inductive bias constructed specifically to discriminate XRD patterns would have a quantum advantage and outperform classical kernels.

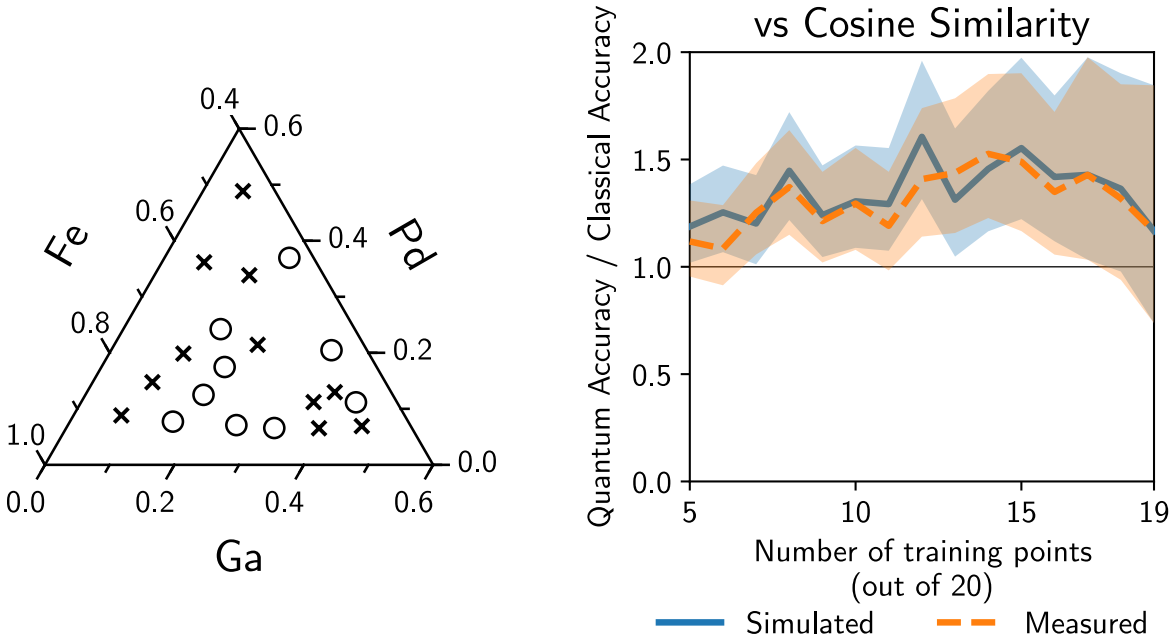



Figure 3.5: The relative performance of the quantum and classical kernels on the engineered labels. The ternary plot on the left shows the engineered labels of the XRD patterns as a function of their composition. Like Figure 3.4, the plot on the right shows the accuracy of the Gaussian process classifier using the quantum kernel relative to the performance the cosine similarity. Again, shaded regions indicate 95 % confidence intervals.

Such a quantum kernel with appropriate inductive bias might be found using the FSL technique of metric learning. The goal of metric learning is to learn a distance or similarity function which can then be used by a simple machine learning model such as k-nearest neighbors [36, 57]. Metric learning techniques could be used to identify or train feature map quantum circuits which produce quantum kernels performant on XRD classification tasks.

Our results should be viewed in the broader context of problem-aware quantum models, where the circuit ansatz is designed to respect known problem structure, as in permutation-equivariant circuits and quantum convolutional architectures [49, 50]. In contrast, our XRD task does not exhibit an obvious global permutation or translational symmetry, so here we restrict attention to a single, generic feature map and analyze its behavior through the model-complexity framework. Systematically exploring symmetry-inspired and task-specific choices of $U$ for diffraction data is an important direction for future work.

## 3.5 Conclusion

In this work, we demonstrated that autonomous materials discovery provides a compelling potential use case for quantum kernel machine learning. Quantum machine learning holds exciting potential for advancing artificial intelligence frameworks, with its success depending critically on aligning the right quantum models with suitable task-data combinations [38]. Building on the theoretical framework of Huang et al. [38], we applied quantum kernels to a real-world supervised x-ray diffraction classification task. We characterized both quantum and classical kernel models using their respective model complexities and performed experiments which demonstrated that quantum kernel models can achieve similar perfor-

mance to classical models while requiring less training data.

## 3.6 Original Author Contributions

In order of size of contribution, beginning with largest contribution; **conceptualization**: equal; **formal analysis**: F.A.; **funding acquisition**: I.T.; **investigation**: F.A.; **methodology**: equal; **software**: F.A., A.G.K.; **supervision**: I.T.; **visualization**: F.A.; **writing / original draft preparation**: F.A.; **writing / review & editing**: equal

# Chapter 4: First-Principles Thermodynamic Analysis of Ternary Chalcogenide Phase Change Materials

## 4.1 Abstract

Chalcogenide phase-change materials (PCMs) are important for nonvolatile memory and reconfigurable photonic technologies. The GeTe – $Sb_2Te_3$ mixture system, commonly referred to as GST, is the most well-known PCM family, but new PCMs are needed to broaden the accessible property space while retaining fast switching. Here, we propose a thermodynamic framework, motivated by Ostwald's rule, for understanding and identifying PCM materials, since direct modeling of phase-transition dynamics is computationally expensive. Using first-principles calculations, we systematically evaluate the energetics of ternary chalcogenide mixtures along binary-binary tie lines and their polymorphs. By comparing ground-state and metastable structures, we assess phase stability, miscibility, and the likelihood of GST-like polymorph-mediated crystallization pathways across a broad composition space. The calculations reproduce known behavior in GST and related systems and identify several promising candidate mixtures with similar features. These results provide insight into why some PCM systems are more favorable than others and establish thermodynamic polymorph screening as a practical route for future PCM discovery.

## 4.2 Introduction

Phase-change materials (PCMs) based on chalcogenide semiconductors can reversibly switch between amorphous and crystalline states while exhibiting large changes in electrical resistance and optical properties [58, 59]. These materials are used for nonvolatile memory and reconfigurable photonic technologies [58–60]. For many applications, rapid amorphous-to-crystalline phase-transition dynamics are essential because they limit the speed of devices. Emerging applications place additional demands on PCM materials. For example, high-temperature embedded computing applications may require crystallization temperatures higher than those of current PCMs to avoid spontaneous crystallization and improve device lifetime [58]. Novel photonic applications seek PCMs with switching behavior over broader wavelength ranges [60]. These needs motivate the discovery and design of new PCM systems that retain fast switching while expanding the accessible property space.

The Ge-Sb-Te ternary system, created by the composition mixture along the tie line of GeTe and $Sb_2Te_3$, commonly referred to as GST, is a well-known PCM system for its combined fast switching dynamics and favorable electrical and optical contrast [58, 59]. Prior studies of GST have identified a metastable rock-salt (RS) phase along its crystallization pathway [61]. GST crystallizes through a two-step process in which the amorphous phase first transforms into a metastable RS structure and then into the ground-state hexagonal phase [61]. The RS phase also contains a high vacancy concentration on the cation sublattice, which gives it substantial tolerance to structural and compositional disorder and may facilitate the amorphous-to-crystalline transition [58, 59]. This RS phase plays a key role in enabling rapid crystallization and can be understood in the context of Ostwald's rule, which states that metastable poly-

morphs may form before the final equilibrium structure because they provide kinetically more accessible transformation pathways [62, 63].

Atomistic simulations based on ab initio molecular dynamics have provided significant insight into amorphous-to-crystalline transformation mechanisms in PCMs [59,64]. However, applying such methods systematically across a broad chemical space is computationally expensive. This challenge motivates the search for simple descriptors that can distinguish materials systems with promising fast phase transition behavior. The GST example suggests that such a descriptor may be viable from a thermodynamic perspective based on Ostwald's rule. If a material system contains a metastable polymorph whose energy lies only slightly above that of the stable crystalline phase, that polymorph may serve as a kinetically favorable intermediate along the crystallization pathway, consistent with Ostwald's rule. Density functional theory (DFT) calculations predict that the RS polymorph of GST lies less than 3 meV / atom above the stable hexagonal phase [65], confirming this thermodynamic interpretation. This framework based on low-energy polymorph may therefore be used for identifying new PCM systems, especially since many chalcogenide compounds exhibit polymorphism. For example, a prior experimental study of GeTe – $Bi_2Te_3$ system also reported the presence of a RS polymorph and fast phase transition behavior [66].

Currently, PCM discovery has remained largely focused on chemical modifications of existing systems, such as doping known compositions or substituting one end-member compound with chemically related analogs [58]. The thermodynamics of mixtures across the broader chalcogenide PCM space remain poorly understood. In particular, there has been no systematic assessment of mixtures along binary-binary tie lines with respect to phase stability, miscibility, and metastable polymorphs. This gap limits both mechanistic understanding and

rational materials discovery.

In this work, we evaluate candidate PCM systems from a thermodynamic perspective, motivated by the Ostwald-like crystallization behavior observed in GST. Using first-principles calculations, we systematically evaluate the energetics of ternary compositions, including ground-state and metastable polymorph phases, along the tie lines of binary-binary mixtures in chalcogenide semiconductors. We compare our results with available experimental literature to validate the approach and to rationalize why some chalcogenide mixtures are more promising PCM candidates than others. By comparing the energies of experimentally known and candidate polymorphs, we identify systems with low-energy meta-stable structures, such as RS-like phases in GST, that could enable fast phase transition.

## 4.3 Results

Candidate ternary PCMs are derived from mixtures of binary chalcogenides. We first identify pairs of binary compositions to mix that are promising for our proposed framework and then generate the corresponding derivative ternary structures for a range of compositions and along the selected tie lines (Section 4.3.1). GST is then examined as a representative system in Section 4.3.2 to validate our approach and the thermodynamic framework motivated by Ostwald's rule. Sections 4.3.3 – 4.3.5 present the calculated results for the remaining candidate systems and their implications.

### 4.3.1 Generation of Candidate Materials

We first identify prospective mixtures of binary chalcogenide compositions in the composition space Si, Ge, Sn, Sb, or Bi with Se or Te, which includes many known PCM systems. For each binary composition, we consider only experimentally known phases or the lowest DFT-energy structures from the Materials Project (MP), and screen them according to the following criteria. Because we focus on ternary mixtures like GST, the two binary compounds must have one element in common. To select mixtures that are more likely to form single-phase materials like GST, at least one polymorph from each binary must belong to the same crystal family. The two binaries must be connected by a tie line (allowing for known ternary compounds along the tie line, e.g. $Ge_2Sb_2Te_5$ between GeTe and $Sb_2Te_3$) using the MP phase diagram based on DFT energies, since otherwise phase segregation would be expected in the mixture. This procedure identifies 30 candidate mixtures (summarized in Table 4.1), including the GeTe – $Sb_2Te_3$ mixture corresponding to the well-known GST system.

In general, most tellurides have a polymorph in the hexagonal crystal family, with close-packed layered structures with octahedral cation coordination (see Figure 4.1 c – e for the relevant GeTe and $Sb_2Te_3$ structures). In contrast, selenides generally have more structurally complex orthorhombic polymorphs with a wider range of coordination environments. For example, orthorhombic $Sb_2Se_3$ (Materials Project ID mp-2160) has an Sb site with square pyramidal coordination, and orthorhombic $Bi_2Se_3$ (Materials Project ID mp-23164) has Bi in square-face capped trigonal prism coordination.

Next, for each candidate mixture, ternary structures were generated over a range of compositions by interpolating between the parent binary compositions along the tie line (Figure 4.1

a). The structures were constructed from the parent binary phases using defect reactions involving cation or anion vacancies (Methods), consistent with the high concentration of cation-site vacancies observed in the RS phase of GST over a wide composition range.

### 4.3.2 GST Polymorph Structures and Energies

Among the 30 candidate mixtures identified (Table 4.1), this procedure correctly recovers the well-known GST system, i.e. the GeTe – $Sb_2Te_3$ mixture (Figure 4.1 a). Figure 4.1 b shows the energies of individual $Ge_2Sb_2Te_5$ structures generated from each of the GeTe or $Sb_2Te_3$ polymorphs. Figure 4.1 f and g show the lowest energy structures of $Ge_2Sb_2Te_5$ derived from the RS (Figure 4.1 c) and hexagonal (Figure 4.1 d) parent binary structures, respectively. The lowest-energy GST structures generated by our algorithm also show the same vacancy ordering and similar Ge and Sb ordering as those by Da Silva et al. [65], confirming our structure

| | GeTe | SnTe | $Sb_2Te_3$ | $Bi_2Te_3$ | $SiTe_2$ | $GeSe_2$ | GeSe | SnSe | $SnSe_2$ | $Sb_2Se_3$ | $Bi_2Se_3$ | $SiSe_2$ |
|---|---|---|---|---|---|---|---|---|---|---|---|---|
| GeTe | | ch | h | h | h | o | co | | | | | |
| SnTe | ch | | h | h | h | | | c | h | | | |
| $Sb_2Te_3$ | h | h | | h | | | | | | | | |
| $Bi_2Te_3$ | h | h | h | | h | | | | | | h | |
| $SiTe_2$ | h | h | | h | | | | | | | | |
| $GeSe_2$ | o | | | | | | | ot | | o | ot | mo |
| GeSe | co | | | | | | | co | | o | o | o |
| SnSe | | c | | | | ot | co | | | o | ot | o |
| $SnSe_2$ | | h | | | | | | | | | h | |
| $Sb_2Se_3$ | | | | | | o | o | o | | | o | o |
| $Bi_2Se_3$ | | | | h | | ot | o | ot | h | o | | o |
| $SiSe_2$ | | | | | | mo | o | o | | o | o | |

Table 4.1: Candidate binary mixtures and their matching crystal families. Crystal families: c=cubic, h=hexagonal, m=monoclinic, o=orthorhombic, t=tetragonal. For mixtures with multiple matching polymorphs, all matching crystal families are shown. Additional selected mixtures are included in the Supplemental Information.

generation approach.

Figure 4.2 a shows the DFT energy as a function of composition for the derived ternary structures in the RS phase of the GST system generated by our algorithm. Figure 4.2 b shows the energy distribution and minimum energy of the RS, hexagonal, and R$\bar{3}$m phases across the GST tie line. The hexagonal-phase ternary mixtures of GeTe and $Sb_2Te_3$ have minimum energies less than 25 meV / atom, which is used in this study as the cutoff for ternary-mixture stability. Our calculations correctly predict that mixtures of GeTe and $Sb_2Te_3$ form single-phase ternary compounds, agreeing with the experimental observation of single-phase ternary compounds like $Ge_2Sb_2Te_5$, $Ge_1Sb_2Te_4$, $Ge_1Sb_4Te_7$, etc [58].

The hexagonal phase is identified as the ground-state structure, and the RS is identified as slightly metastable with energy difference of $< 10$ meV / atom, in agreement with the experimental observations [61] and previous results [65]. By contrast, the ternary mixture derived from the R$\bar{3}$m $Sb_2Te_3$ phase is far above the 25 meV / atom cutoff. These results are consistent with experiments and support Ostwald's rule explanation for the crystallization pathway of GST, that the metastable RS phase crystallizes first followed by the ground-state hexagonal phase [61–63].

### 4.3.3 Telluride Mixtures

Here we present the results of our calculations for the remaining telluride candidate mixtures. Figure 4.3 shows the energy of different polymorphs as a function of composition for the multi-cation telluride systems, with the GST system shown in the first row, second column, as a simplified version of Figure 4.2 b.

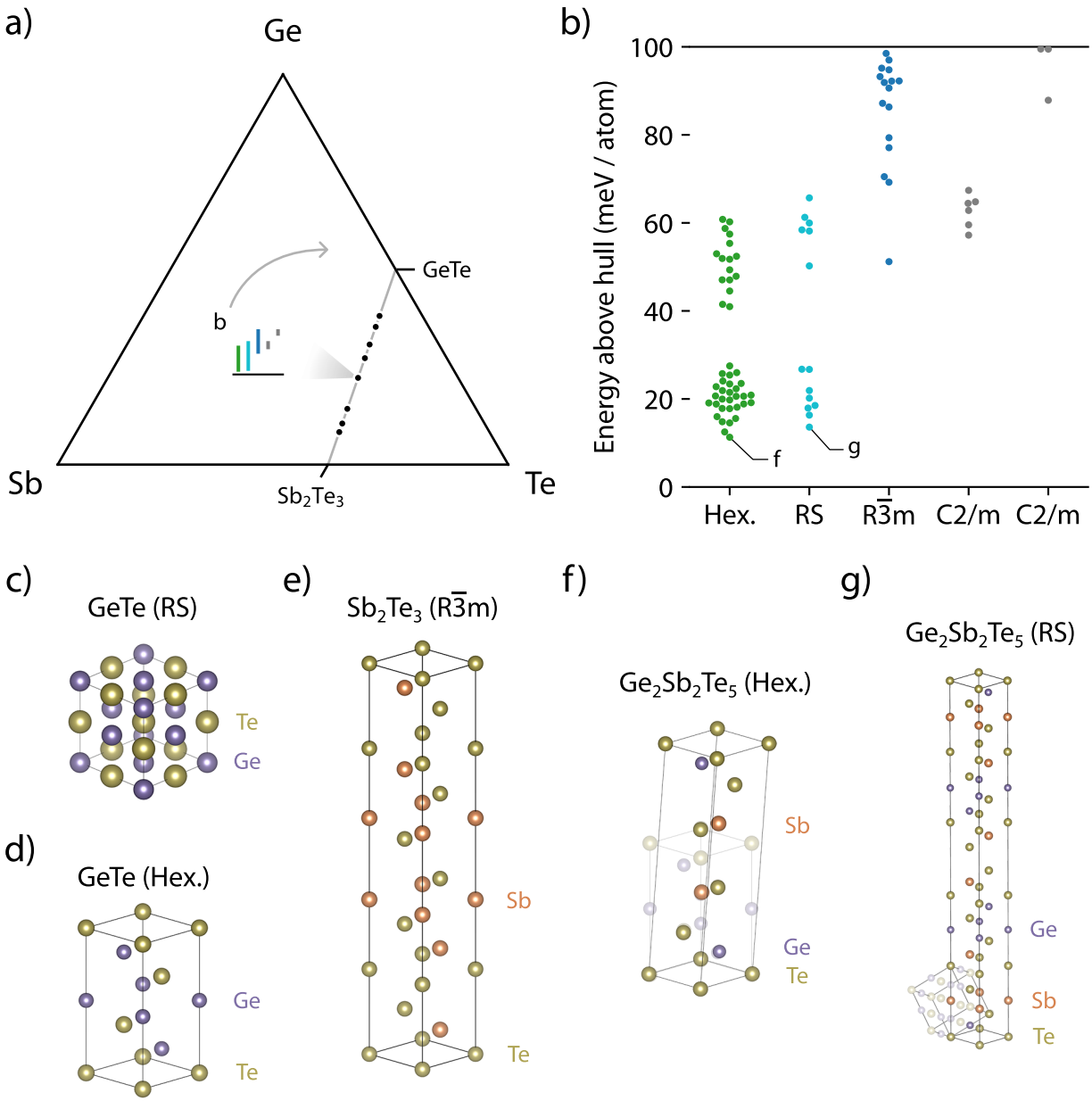


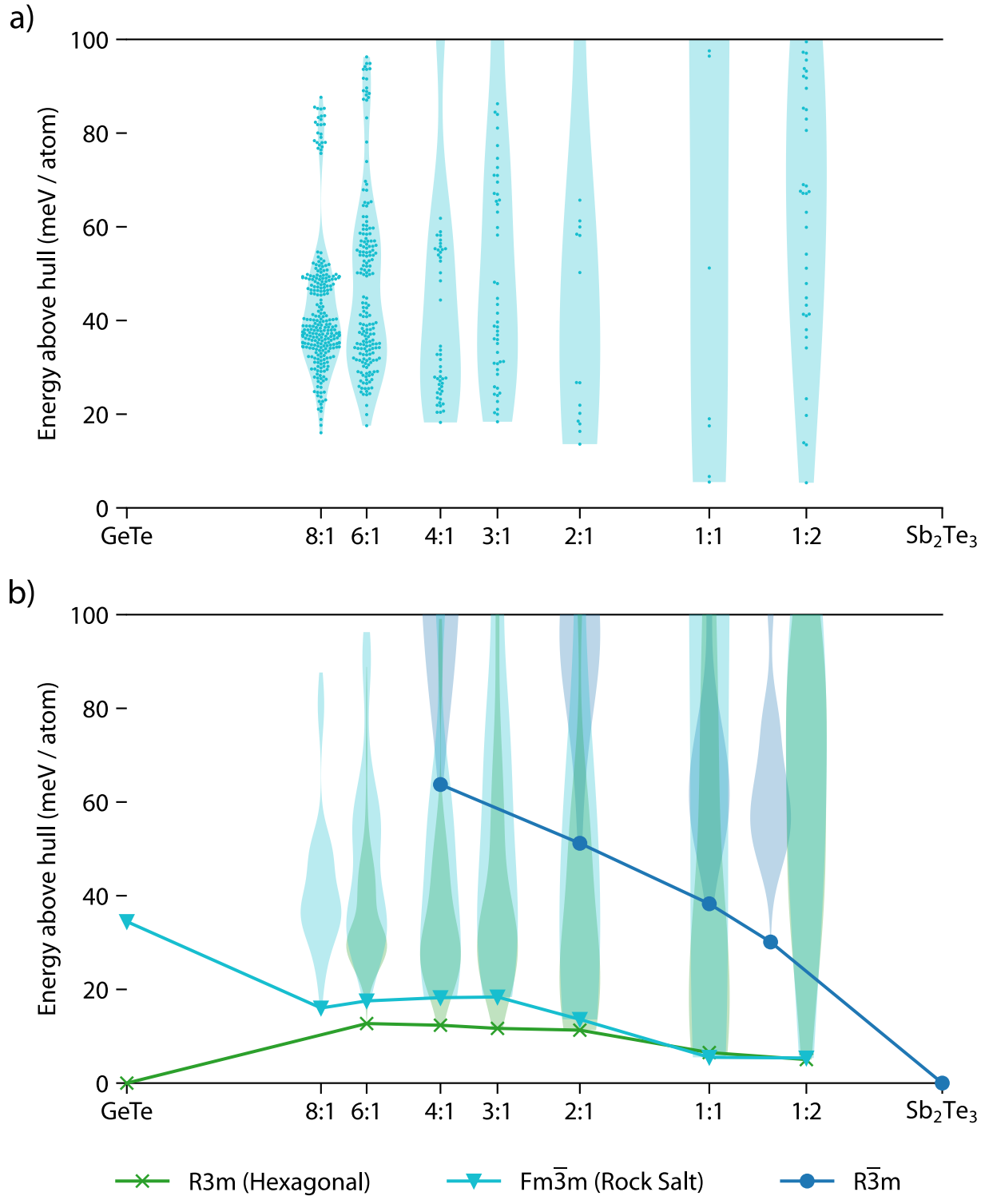

Figure 4.1: a) The Ge-Sb-Te ternary composition space, showing the GeTe – $Sb_2Te_3$ tie line and select mixing compositions. b) The energies of structures in different phases of $Ge_2Sb_2Te_5$. c) Rock salt GeTe structure. d) Hexagonal GeTe structure. e) Hexagonal $Sb_2Te_3$ structure. f) The lowest-energy generated $Ge_2Sb_2Te_5$ structure in the hexagonal phase. g) The lowest-energy generated $Ge_2Sb_2Te_5$ structure in the rock salt phase. The translucent structures overlaid on f and g are the parent structures d and c.

The GeTe – $Bi_2Te_3$ mixture has the same phases as GST. The hexagonal phase mixture energies are in the range of 15 to 25 meV / atom, and RS phase mixtures are 15 to 35 meV / atom, and R$\bar{3}$m phase mixtures are much higher at 40 to 75 meV / atom. Similar to GST, our calculations indicate single-phase formation in this mixture, and a kinetically accessible RS phase 0 to 10 meV / atom higher in energy than the hexagonal phase. This agrees with experimental observations that this system has been synthesized without phase segregation, including compositions with $< 50$ % $Bi_2Te_3$ [66]. Experiments also find either the amorphous or RS phase as deposited and the hexagonal phase upon annealing [66]. Experiments also show this system has similar crystallization times as GST [66], supporting our Ostwald-rule framework.

In the GeTe – SnTe mixture, the hexagonal phase is consistently below 25 meV / atom, while the energy of the ternary RS phase is about 25 to 50 meV / atom, decreasing monotonically as a function of SnTe fraction. Experimentally, GeTe and SnTe form a continuous solid solution, in agreement with the consistently low energy of the hexagonal phase [67]. The low energy of the metastable RS polymorph phase corresponds with an increase in crystallization speed; in agreement with the crystallization measurements of this mixture that adding SnTe accelerates the crystallization of GeTe [68].

In the $Sb_2Te_3$ – $Bi_2Te_3$ mixture, the common polymorph, the R$\bar{3}$m phase, has a uniformly

Figure 4.2: a) The energies of ternary structures in the rock salt phase along the GeTe – $Sb_2Te_3$ tie line. Each vertical group corresponds to the composition below it, with some horizontal jitter added to prevent overlapping. The violin plots show the kernel density estimate of the energy distribution. b) The energy distributions (violin plot) and minimum energies (marker) as a function of composition for the rock salt, hexagonal, and R$\bar{3}$m phases of GST. Energies above 100 meV / atom are not shown for clarity.

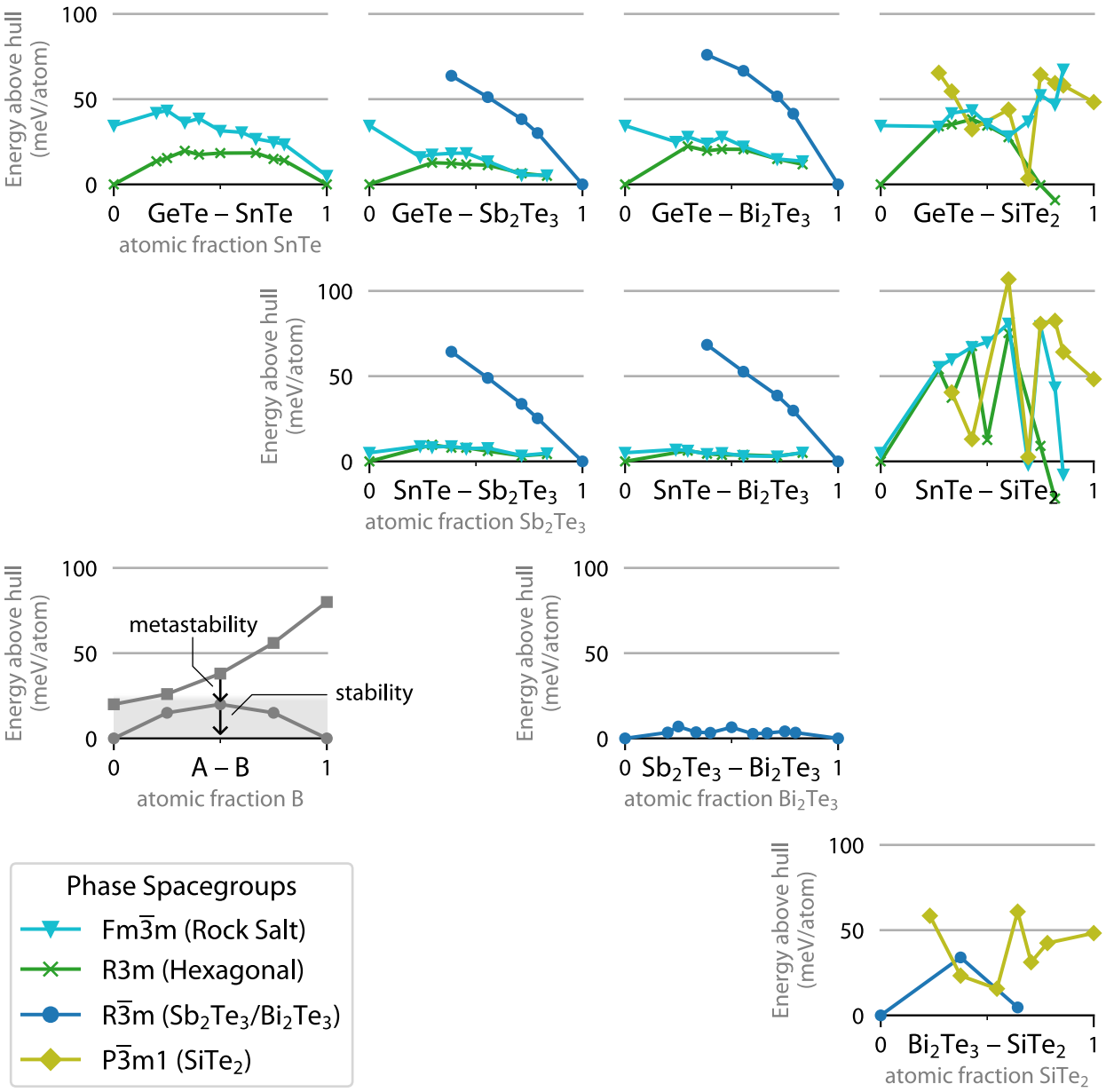

a)
b)
Energy above hull (meV / atom)
100
80
60
40
20
0
GeTe
8:1
6:1
4:1
3:1
2:1
1:1
1:2
Sb2Te3
R3m (Hexagonal)
Fm3̄m (Rock Salt)
R3̄m

low energy < 10 meV / atom across the entire composition range, suggesting a solid solution. Indeed, a solid solution with the R$\bar{3}$m structure is observed experimentally [69]. No other polymorphs, such as a RS phase, were reported in the experiments with increasing quench rate [69], in agreement with the single low-energy phase predicted in our computation (Figure 4.3). The lack of a RS-like polymorph suggests $Sb_2Te_3$ – $Bi_2Te_3$ wouldn't have fast, GST-like crystallization. Indeed, optical PCM experiments with this mixture required long laser irradiation times of 40 $\mu$s to achieve the crystalline state [70].

The last column of Figure 4.3 contains mixtures of GeTe, SnTe, and $Bi_2Te_3$ with $SiTe_2$. These candidate mixtures exhibit erratic DFT energy across the tie-line. $SiTe_2$ is predicted to decompose into Si and Te using the r$^2$SCAN functional, so its endpoint lies above the horizontal axis. The presence of low energy compositions ($< -10$ meV / atom) among high energy compositions ($> 50$ meV / atom) suggests that specific ordered structures are stable, but with limited compositional and structural flexibility. These materials are thus likely to not have the phase transition behavior as we expect from our Ostwald rule perspective. There is no experimental exploration of these mixtures in the PCM literature.

For the SnTe – $Sb_2Te_3$ and SnTe – $Bi_2Te_3$ mixtures, both the hexagonal and RS phases have energies below 10 meV / atom and their difference in energy is negligible, suggesting

Figure 4.3: The minimum DFT energies of ternary structures in each phase as a function of composition along telluride tie lines. The schematic illustrates the stability and metastability of ternary phases with the 25 meV / atom cutoff (the gray shaded region) for stability, above which ternary compositions are expected to phase segregate into their parent binary compositions. Rows and columns correspond to the left and right binary compositions, respectively, ordered as: GeTe, SnTe, $Sb_2Te_3$, $Bi_2Te_3$, and $SiTe_2$. Horizontal axes are in units of atomic fraction of the right-hand composition.


Energy above hull (meV/atom)
100
50
0
0 GeTe – SnTe 1
atomic fraction SnTe
0 GeTe – Sb2Te3 1
0 GeTe – Bi2Te3 1
0 GeTe – SiTe2 1
0 SnTe – Sb2Te3 1
atomic fraction Sb2Te3
0 SnTe – Bi2Te3 1
0 SnTe – SiTe2 1
metastability
stability
0 A – B 1
atomic fraction B
0 Sb2Te3 – Bi2Te3 1
atomic fraction Bi2Te3
0 Bi2Te3 – SiTe2 1
atomic fraction SiTe2
Phase Spacegroups
Fm3̄m (Rock Salt)
R3m (Hexagonal)
R3̄m (Sb2Te3/Bi2Te3)
P3̄m1 (SiTe2)

that ternary compositions can form single phase. In agreement, single-phase ternary compounds with the same layered structures as the GST compounds (Figure 4.1) are experimentally reported [71, 72]. In the literature, nearby mixtures $Sn_xTe_{100-x}$ ($x < 0.35$) – $Sb_2Te_3$ were reported to have similar layered structures as GST and required less power to switch compared to GST [73]. Consistent with the Ostwald-rule framework, these results suggest SnTe – $Sb_2Te_3$ and SnTe – $Bi_2Te_3$ are promising candidate mixtures.

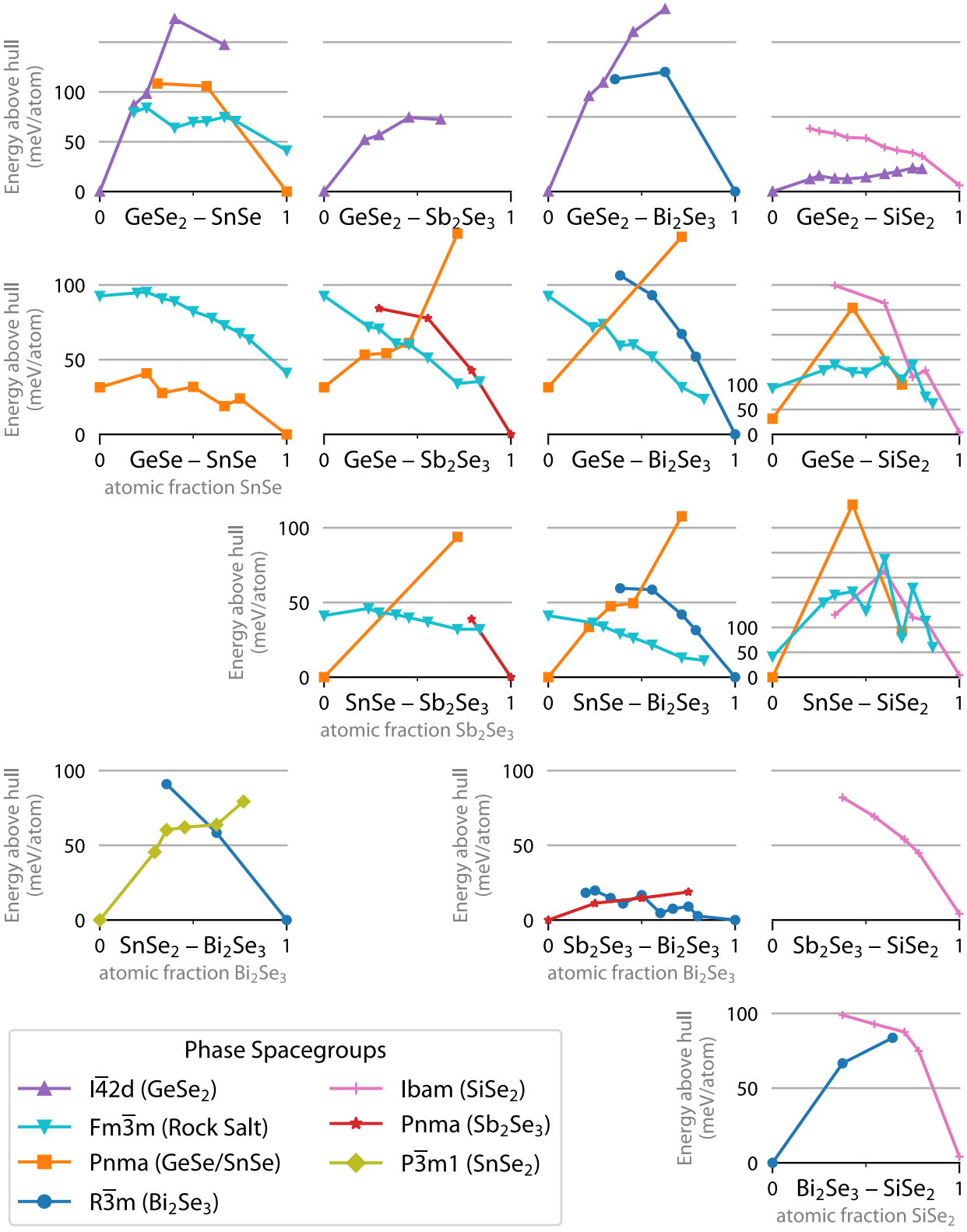
### 4.3.4 Selenide Mixtures

Figure 4.4 shows the energy of different polymorphs in the candidate selenide mixtures. The selenides generally have higher energies above hull than the tellurides and more diverse structures. Many of the parent binary structures have large primitive unit cells (e.g., 20 atoms for $Sb_2Se_3$), which limits the accessible compositions.

The GeSe – $Sb_2Se_3$ mixture is the selenide analogue of GST. GeSe is predicted to not be on the energy convex hull by the r$^2$SCAN functional. DFT predicts all ternary polymorphs have energy above 40 meV / atom, indicating likely phase separation. Non-RS polymorph phases are also high in energy (> 50 meV / atom). GeSe – $Sb_2Se_3$ does not exhibit the thermodynamic features that our framework identifies as favorable for fast-switching PCM behavior, and is known to be a poor PCM, with little appearance in the PCM literature.

The ternary compositions in the $GeSe_2$ – SnSe, $GeSe_2$ – $Sb_2Se_3$, and $GeSe_2$ – $Bi_2Se_3$ mix-

Figure 4.4: The minimum DFT energies of ternary structures in each phase as a function of composition along selenide tie lines. Rows and columns correspond to the left and right binary compositions, respectively, ordered as: $GeSe_2$, GeSe, SnSe, $Sb_2Se_3$, $Bi_2Se_3$, and $SiSe_2$. Horizontal axes are in units of atomic fraction of the right-hand composition.


Energy above hull (meV/atom)
100
50
0
0 GeSe$_2$ – SnSe 1
0 GeSe$_2$ – Sb$_2$Se$_3$ 1
0 GeSe$_2$ – Bi$_2$Se$_3$ 1
0 GeSe$_2$ – SiSe$_2$ 1
0 GeSe – SnSe 1
0 GeSe – Sb$_2$Se$_3$ 1
0 GeSe – Bi$_2$Se$_3$ 1
0 GeSe – SiSe$_2$ 1
atomic fraction SnSe
0 SnSe – Sb$_2$Se$_3$ 1
0 SnSe – Bi$_2$Se$_3$ 1
0 SnSe – SiSe$_2$ 1
atomic fraction Sb$_2$Se$_3$
0 SnSe$_2$ – Bi$_2$Se$_3$ 1
0 Sb$_2$Se$_3$ – Bi$_2$Se$_3$ 1
0 Sb$_2$Se$_3$ – SiSe$_2$ 1
atomic fraction Bi$_2$Se$_3$
0 Bi$_2$Se$_3$ – SiSe$_2$ 1
atomic fraction SiSe$_2$
Phase Spacegroups
I$\bar{4}$2d (GeSe$_2$)
Fm$\bar{3}$m (Rock Salt)
Pnma (GeSe/SnSe)
R$\bar{3}$m (Bi$_2$Se$_3$)
Ibam (SiSe$_2$)
Pnma (Sb$_2$Se$_3$)
P$\bar{3}$m1 (SnSe$_2$)

tures all have high energies 40 meV / atom or higher, indicating phase separation. Experimentally, $GeSe_2$ mixtures have mostly been studied for their glass-forming ability and generally phase segregate upon crystallization [74–76], in agreement with the DFT results, making them poor PCMs.

For GeSe – SnSe mixture, the energies of the ternary orthorhombic phase are between 25 to 50 meV / atom, while the RS phase is between 50 to 100 meV / atom. These results indicate that the orthorhombic phase may form solid solution over a part of composition range, and the RS phase is likely too high in energy to appear during crystallization, preventing fast crystallization. An experiment with $Ge_2Se_3$ / SnSe stacks (similar to GeSe – SnSe mixtures) reported switching behavior when the two compounds were made to alloy, but no measurements of crystallization speed were reported [77].

The trends of polymorph energies in GeSe – $Bi_2Se_3$ are similar to those of GeSe – $Sb_2Se_3$. The ternary compositions have energies above hull of 30 meV / atom, indicating likely phase segregation. This mixture, similar to GeSe – $Sb_2Se_3$, is not expected to be good a PCM and has little appearance in the PCM literature.

SnSe – $Sb_2Se_3$ also appears similar to GeSe – $Sb_2Se_3$. SnSe shares the same orthorhombic and RS polymorphs as GeSe but is predicted to be on the convex hull by the r$^2$SCAN functional. The energies of some SnSe-based polymorphs are up to 30 meV / atom lower than in GeSe – $Sb_2Se_3$, though still above 40 meV / atom. Single-phase ternary compounds (e.g. $Sn_2Sb_2Se_5$) with orthorhombic structures have been found experimentally [78]. Overall, SnSe – $Sb_2Se_3$ mixture does not satisfy the thermodynamic features of our framework.

Unlike $Sb_2Te_3$ – $Bi_2Te_3$ mixture, the selenides $Sb_2Se_3$ and $Bi_2Se_3$ don't share the same ground state polymorph. The ternary structures from both polymorphs of this mixture have

energies consistently below 25 meV / atom, increasing as the composition deviates from their parent binaries. The calculated energies indicate the favorable ground state structure changes near the middle of the tie line, consistent with the experimental observation of the phase change near 70 % $Bi_2Se_3$ [79]. The DFT results do not show the thermodynamic features of our framework, which may help explain the limited reports on the PCM behavior of this system in the literature.

The $GeSe_2$ – $SiSe_2$ ternary compositions have much lower energies compared to the other mixtures with either $GeSe_2$ or $SiSe_2$. Like $Sb_2Se_3$ – $Bi_2Se_3$, the two binaries have different ground state polymorphs. The energy of the $GeSe_2$ polymorph (10 to 25 meV / atom) is consistently below that of the $SiSe_2$ polymorph (25 to 45 meV / atom). As suggested by these DFT results, a single-phase mixture based on the tetragonal $GeSe_2$ phase may form over a range of this composition on the tie line, with the $SiSe_2$-derived mixture polymorph with a close energy over a narrow composition range. This behavior is distinct from the low-energy metastable polymorph landscape targeted by our framework, and we therefore do not expect this mixture to exhibit GST-like fast-switching behavior.

$SiSe_2$ mixtures have similar results to their $GeSe_2$ counterparts. SnSe – $SiSe_2$, $Sb_2Se_3$ – $SiSe_2$, $Bi_2Se_3$ – $SiSe_2$, and GeSe – $SiSe_2$ all have very high ($> 50$ meV / atom) energies for their ternary structures. These mixtures likely behave like most of the $GeSe_2$ mixtures, including a tendency towards phase segregation. This is consistent with an experimental study of Si doping in GST, in which Si was found to separate into a Si-rich phase [80]. Similarly, experimental studies of Si-doped $Sb_2Se_3$ find that Si phase-segregates upon recrystallization, forming a nanocomposite of $Sb_2Se_3$ grains in an amorphous Si-rich matrix [81], consistent with the high predicted energies for similar $Sb_2Se_3$ – $SiSe_2$ mixtures in our calculations. Although in these

studies, such Si-rich phase separation may reduce the reset power of PCM devices by acting as high-resistance micro heaters [80] or enable tailoring of optical phase-change properties [81], this is not the GST-like behavior targeted by our framework for a fast-switching PCM.

The $SnSe_2$ – $Bi_2Se_3$ mixture is the only selenide candidate mixture with a hexagonal crystal family match, like the tellurides, but the energy results are similar to those of other selenides. The ternary compositions have high energies above 50 meV / atom, indicating phase separation. Indeed, experiments find this mixture has limited solubility [82]. Unlike the SnSe – $Bi_2Se_3$ system, this system also does not show a low-energy RS polymorph. Thus, we do not expect it to exhibit GST-like PCM behavior.

Among these selenide mixtures, SnSe – $Bi_2Se_3$ mixture shows the thermodynamic features similar to GST. In this mixture, the energy of the RS polymorph phase is low at about 20 meV / atom, on par with GST. Single-phase ternary compounds have been found in this system as well (e.g. $Sn_4Bi_2Se_7$), and with RS structures like those of the GST compounds [83]. SnSe – $Bi_2Se_3$ doesn't appear in the PCM literature, but the energy fits our framework and may be a promising PCM candidate mixture among the selenides.

Overall, the selenide mixtures have higher energies and are thus more likely to phase segregate that the tellurides. Selenides also show fewer low-energy polymorphs than tellurides, and their polymorphs are generally higher in energy. As a result, they generally do not exhibit the features identified in GST and targeted by our framework. These factors may help explain why selenides appear less frequently than tellurides as PCMs in the literature.

### 4.3.5 Multi-Anion Mixtures

Lastly, we present the results for mixtures of selenides and tellurides in Figure 4.5. We consider only mixtures in which the cation valence does not change, which excludes GeTe – $GeSe_2$ and SnTe – $SnSe_2$.

For GeTe – GeSe, the energies of the ternary compositions are above 25 meV / atom due to the high energy of GeSe. The lowest energy structure transitions from the hexagonal GeTe phase to the orthorhombic GeSe phase, while the RS phase remains consistently 40 meV / atom above the hexagonal phase, reaching 60 to 100 meV / atom. This suggests that as the concentration of GeSe increases, this mixture is more likely to phase segregate and less likely to exhibit the RS phase. Experimentally, mixtures with up to 70 % GeSe have been demonstrated, and the addition of GeSe significantly slows crystallization speed [68], in agreement with the increasing energy of the RS phase.

The $Bi_2Te_3$ – $Bi_2Se_3$ predictions look nearly identical to those of the $Sb_2Te_3$ – $Bi_2Te_3$ system. These two binaries also have the same structure, and the ternary compositions between them all have low energies below 10 meV / atom, indicating a favorable solid solution. Like $Sb_2Te_3$ – $Bi_2Te_3$, there is no metastable polymorph present to facilitate fast crystallization. $Bi_2Te_3$ – $Bi_2Se_3$ solid solutions have been experimentally demonstrated for thermoelectric and optical applications [84], but don't appear in the PCM literature.

Like GeTe – GeSe, the SnTe – SnSe mixture shows a transition in the lowest energy phase be-tween the hexagonal and orthorhombic phases, but the ternaries compositions are much lower in energy (20 to 50 meV / atom). The energy of the RS phase is 25 to 50 meV / atom, only a few meV / atom above the hexagonal phase. These results suggest that this mixture may form

the RS phase if the concentration of SnSe is not too high. This system exhibits the thermodynamic features targeted by our framework, although phase segregation may be likely due to the relatively high energies. In agreement, differential scanning calorimetry measurements of $Sn_xSe_{80-x}Te_{20}$ glasses showed multi-step crystallization, like GST [85], and phase segregation was also observed [85].

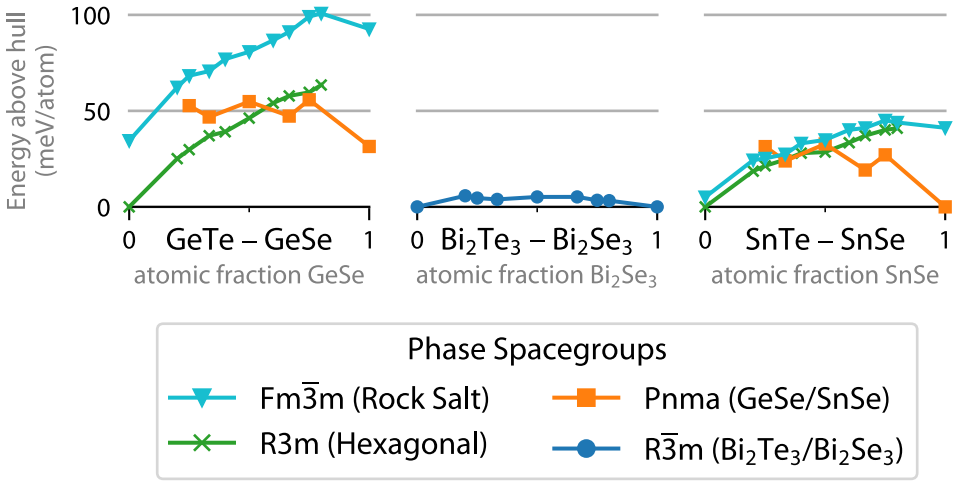



Figure 4.5: The minimum DFT energies of ternary structures in each phase as a function of composition along multi-anion tie lines. Horizontal axes are in units of atomic fraction of the right-hand composition.

## 4.4 Discussion

In this work, we examined ternary chalcogenide mixtures from a thermodynamic perspective motivated by the Ostwald-like crystallization behavior of GST. Within this framework, fast-switching PCM candidates are expected to exhibit both a low-energy ground-state crystalline phase and also a low-energy metastable polymorph, particularly a RS-like phase, that may provide a kinetically accessible intermediate during crystallization. The results for the GST system serves as a validation for this framework. Our calculations correctly identify the

hexagonal phase as the ground state and the RS phase as slightly metastable, in agreement with prior calculations and experiments. Similarly, the calculations reveal the favorable low-energy polymorph landscape of the GeTe – $Bi_2Te_3$ system, which is also consistent with fast-switching behavior observed experimentally. These thermodynamic analyses also correctly reproduce several known behaviors in mixed chalcogenide systems, including the ground-state structures, phase transitions, solid-solution formation, and tendency to phase segregate. It also shows that selenides generally lie higher in energy, are more prone to phase segregation, and less often exhibit favorable low-energy polymorphs, which may help explain why they are less common than tellurides in the PCM literature. These agreements suggest that these first-principles thermodynamics analyses of the polymorph energetics provide a useful framework for rationalizing why some binary-binary mixtures are more favorable than others and for identifying potential PCM systems.

Guided by this framework, several mixtures emerge as promising candidates for further exploration. In particular, SnTe – $Bi_2Te_3$ and SnSe – $Bi_2Se_3$ both exhibit low-energy RS phases comparable to those of known fast-switching systems, and SnTe – SnSe shows a substantially lower RS energies than GeTe – GeSe. These systems are also experimentally accessible, as reported in thermoelectric literature, and merit experimental evaluation for PCM-relevant properties, including crystallization kinetics, cyclability, and application-relevant optical or electrical contrast.

The trends observed across the composition space also suggest a broader structural design principle. Binary parent phases with octahedral coordination environments similar to those of RS-derived structures are more likely to yield low-energy RS-like ternary polymorphs. For example, the SnSe – $Sb_2Se_3$ system with only orthorhombic parent structures with differ-

ent or highly distorted octahedral coordination compared to the SnSe – $Bi_2Se_3$ system, which benefits from the hexagonal $Bi_2Se_3$ parent structure which has RS-like octahedral coordination. This difference is consistent with the much more favorable RS-like polymorph landscape predicted for SnSe – $Bi_2Se_3$.

These results suggest that future PCM discovery efforts may extend beyond the binary compositions studied here by targeting mixtures whose parent compounds share compatible octahedral structural motifs, such as $TiTe_2$ with GeTe and $Sb_2Te_3$. The computational framework can also be extended to mixtures of three binaries or even higher component systems. For example, our results suggest that quaternary PCMs, such as GeTe – SnTe – $Sb_2Te_3$, combine mutually compatible binary mixtures and may exhibit the favorable polymorph features.

While we focus on identifying single-phase materials in this work, phase segregation can in some cases be used beneficially for tailoring PCM properties [81]. For example, recent work on Si-incorporated $Sb_2Se_3$ showed that phase segregation into nanocomposites can be exploited as a design strategy for tuning optical phase change behavior. Although phase segregation is generally unfavorable within our GST-inspired framework for identifying fast-switching single-phase PCM systems, this requirement varies by the target application. This suggests a broader direction for future materials discovery, in which phase segregating systems may also be explored intentionally when the goal is to engineer optical, thermal, or other properties rather than replicating GST-like fast switching mechanisms.

Further improvement can be made to the limitations in the current computation approach. First, the DFT calculations are performed at 0 K and do not explicitly include temperature effects. To incorporate temperature effects based on experimental conditions, temperature-dependent descriptors [86] or statistical approaches based on Monte Carlo sim-

ulations may be conducted [87]. Second, the present analysis evaluates energies relative to the convex hull of crystalline phases, and the relative energies between amorphous and crystalline phases are not captured directly. Incorporating amorphous structures would provide additional insight, but obtaining reliable amorphous configurations generally requires computationally demanding molecular dynamics simulations. The present work focuses on thermodynamic polymorph landscapes and does not directly compute crystallization kinetics [88], although there is the potential to extract some kinetic information from the energy distributions of the ordered ternary structures. Molecular dynamics simulations may also be used to directly study the phase transition mechanisms, including the nucleation and growth of the crystalline phase from the amorphous state [89], providing detailed mechanisms of crystallization kinetics in promising candidate systems identified by our framework. Application-relevant functional properties, including resistivity or optical contrast, are also not calculated. These remain important directions for future work.

## 4.5 Methods

### 4.5.1 Candidate Binary Selection

We collected the candidate binary structures from the Materials Project [90]. We excluded non-stoichiometric compositions, such as $SbTe_2$, which approximates the Sb – Te eutectic composition $Sb_{30}Te_{70}$, because they are unlikely to behave like the stoichiometric binary parent compounds GeTe and $Sb_2Te_3$ which form GST.

To identify whether a pair of binary compositions is connected via a tie line in the 0 K DFT-predicted phase diagram, we use a combination of graph search and tools from py-

matgen [91]. We construct the DFT phase diagram using the phase diagram tool from pymatgen [92,93] all the Materials Project entries in the relevant composition space. We then convert the phase regions in the phase diagram into a graph, in which tie lines are edges connecting composition vertices. We next use the A* algorithm [94] to find the shortest path between the two binary composition nodes in the graph. If all compositions on the shortest path between the two binaries were collinear, the two binaries were considered to be connected by a tie line, and were retained as a candidate pair.

Some binary compounds, such as $SiTe_2$, GeSe, and $BiSe_2$, are only predicted to be on the convex hull using GGA functional calculations and are predicted to be unstable by higher fidelity $r^2$SCAN [95] calculations. We still consider these compositions.

### 4.5.2 Vacancy Charge Compensation

When interpolating between the binary compositions to produce ternary compositions, we automatically determined the appropriate vacancy defect reaction for charge balancing based on the oxidation states of the relevant species. If the dopant and substituted species have the same oxidation state, no charge compensation is required. If the oxidation state of the dopant species is greater in magnitude than that of the substituted species, then additional vacancies are added on the substituted species sublattice. Otherwise, vacancies are added to the other sublattice of the binary structure. If there are multiple possible substituted species, due to cation multi-valence, we ignore these structures as they would require a more complex ordering scheme. The resulting compositions of the ternary structures were limited to simple stoichiometric ratios with denominators less than 6 (e.g., $Ge_2Sb_2Te_5$ and not $Ge_7Sb_8Te_{19}$) and

to compositions achievable with less than 100 atoms.

### 4.5.3 Ternary Structure Ordering

Given the ternary compositions and parent binary structures, we used EnumLib [96] via pymatgen to generate the ternary structures. The cation and anion sublattices of the parent structures were updated with the fractional occupation of the three species in the ternary composition. Then EnumLib was used to enumerate all the symmetrically distinct atomic orderings with the minimum supercell size. We determined the possible compositions and their required minimum supercell size using the procedure outlined in pseudocode in Figure 4.6. We only considered compositions with simple stoichiometric ratios (i.e., with a denominator of less than 6). After ordering, we discarded composition-structure combinations with more than 1,000 ordered structures because they were not computationally practical for DFT calculations.

```
structures = {}
compositions = {}
sizes = {}

for all supercell sizes such that the number of atoms is < 100:
    for all defect reaction multiples that fit in the supercell:
        determine the number of each species
        calculate the corresponding dopant / substituted fraction
        if the fraction is simple and not in compositions:
            assign the fractional occupancy to the parent structure
            add the resulting unordered structure to structures
            add the composition to compositions
            add the supercell size to sizes
```

Figure 4.6: Algorithm pseudocode for determining ternary compositions and required supercell sizes, given a dopant species and a parent binary structure.

### 4.5.4 DFT Calculations

We performed the DFT calculations using a combination of Perdew – Burke – Ernzerhof (PBE) [97] and r$^2$SCAN [95] calculations. The ordered ternary structures generated by EnumLib were first relaxed using the less expensive PBE functional, then the more expensive r$^2$SCAN functional was used to calculate a more accurate energy of the relaxed structure.

The DFT calculations were performed with the Vienna Ab initio Simulation Package (VASP) [98]. All calculations were performed using automatically generated Materials Project compatible VASP inputs created by pymatgen [91]. The ternary structure energy values reported in this work were calculated with respect to the entries in the Materials Project [90], also calculated using pymatgen [91].

## 4.6 Original Author Contributions

**Felix Adams**: Conceptualization, Methodology, Software, Validation, Formal Analysis, Investigation, Data Curation, Writing – Original Draft, Visualization; **Ichiro Takeuchi**: Conceptualization, Supervision, Funding Acquisition; **Carlos Ríos Ocampo**: Conceptualization, Supervision, Funding Acquisition; **Yifei Mo**: Conceptualization, Methodology, Resources, Writing – Review & Editing, Supervision, Funding Acquisition.

# Chapter 5: Summary and Future Work

## 5.1 Summary

Chapter 2 presents a technique for human-artificial intelligence collaboration in the field of autonomous materials phase mapping and shows that by drawing boundaries and regions on predicted phase maps, human experts can meaningfully accelerate an autonomous experiment. Chapter 3 explores a compelling potential use case for quantum kernel machine learning in autonomous materials discovery and demonstrates that quantum kernel models can require less training data than classical kernel models for a specific supervised x-ray diffraction classification task. Chapter 4 conducts thermodynamic analyses based on density functional theory for searching for candidate ternary phase change materials and identifies several promising Sn-based mixtures which are underexplored in the phase change material literature.

Taken together, these works illustrate several ways computation can be used to facilitate data-driven materials discovery. Each project takes a different approach, but they share a common goal of accelerating the discovery of new materials. All of these approaches: improving machine learning interpretability, reducing machine learning training data requirements, identifying candidate materials, and complementary components for solving the challenge of navigating the space of possible materials.

## 5.2 Future Work

For each of the studies in this thesis, there are opportunities to continue building on the finished work. For Chapter 2, one could explore integrating human input into the automated analysis of the x-ray diffraction patterns from which phase maps are constructed. For Chapter 3, one could explore additional quantum kernel feature map circuits that are specifically constructed for materials science data. For Chapter 4, one could further expand the composition space in which the search for candidate materials is performed. The broader challenge, however, is not only to improve each of these individual approaches, but also to integrate them into a cohesive materials-discovery framework. The full potential of data-driven materials discovery will likely require combining high-throughput experiments, computation, machine learning, and autonomous decision-making into unified workflows that can efficiently identify, characterize, and optimize new materials.

# Publications

Felix Adams, Austin McDannald, Ichiro Takeuchi, and A. Gilad Kusne. Human-in-the-loop for Bayesian autonomous materials phase mapping. *Matter*, 7(2):697–709, February 2024

Felix Adams, Daiwei Zhu, David W. Steuerman, A. Gilad Kusne, and Ichiro Takeuchi. Quantum kernel machine learning for autonomous materials science. *APL Quantum*, 3(1):016115, 03 2026

Felix Adams, Ichiro Takeuchi, Carlos Ríos Ocampo, and Yifei Mo. First-Principles Thermodynamic Analysis of Ternary Chalcogenide Phase Change Materials. *In Writing*. 2026

Chih-Yu Lee, Yi-Siou Huang, Felix Adams, Chuanyu Lian, Hongyi Sun, Jie Zhao, Zichao Ye, Nathan Youngblood, Juejun Hu, Leslie H Allen, Yifei Mo, Ichiro Takeuchi, and Carlos A Ríos Ocampo. Incorporating Si into Sb2Se3: Tailoring Optical Phase Change Materials via Nanocomposites. *Advanced Optical Materials*, 14(8):e03389, 2026

# Appendix A: Supplemental Information for Quantum Kernel Machine Learning for Autonomous Materials Science

## A.1 Calculation of Model Complexity and Geometric Difference

In order to calculate the geometric difference and model complexity using the equations in Ref. [38], we used the Singular Value Decomposition as implemented in NumPy:

```
import numpy as np

# calculate the SVD of the classical and quantum matrices
cU, cS, cVh = np.linalg.svd(classical_kernel_matrix, hermitian=True)
qU, qS, qVh = np.linalg.svd(quantum_kernel_matrix, hermitian=True)

# use the SVD to calculate the square root and inverse matrices
sqrt_qK = qU @ np.diag(np.sqrt(qS)) @ qVh
inv_cK = cVh.T @ np.diag(cS**(-1)) @ cU.T

# calculate the singular values of the prescribed matrix product
tS = np.linalg.svd(sqrt_qK @ inv_cK @ sqrt_qK, compute_uv=False)

# calculate the geometric difference from the singular values
g_cq = np.sqrt(np.max(tS))

# calculate the other inverse matrix
inv_qK = qVh.T @ np.diag(qS**(-1)) @ qU.T

# calculate the model complexities
s_C = 0
s_Q = 0

for i in range(inv_cK.shape[0]):
    for j in range(inv_cK.shape[1]):
        s_C += inv_cK[i, j] * (1 if true_labels[i] == true_labels[j] else -1)
        s_Q += inv_qK[i, j] * (1 if true_labels[i] == true_labels[j] else -1)
```

## A.2 Construction of Engineered Labels

Similarly, we use the construction from the supplemental information of Ref. [38] to create the engineered labels.

```
# calculate the eigenvalues and eigenvectors of the prescribed matrix
product eig_vals, eig_vecs = np.linalg.eig(sqrt_qK @ inv_cK @ sqrt_qK)

# threshold the values in the eigenvector with the largest eigenvalue to create the labels
engineered_labels = np.array([0 if x < 0 else 1 for x in sqrt_qK @ eig_vecs[:, 0]])
```

## A.3 Kernel Matrices and Performance Data Replots

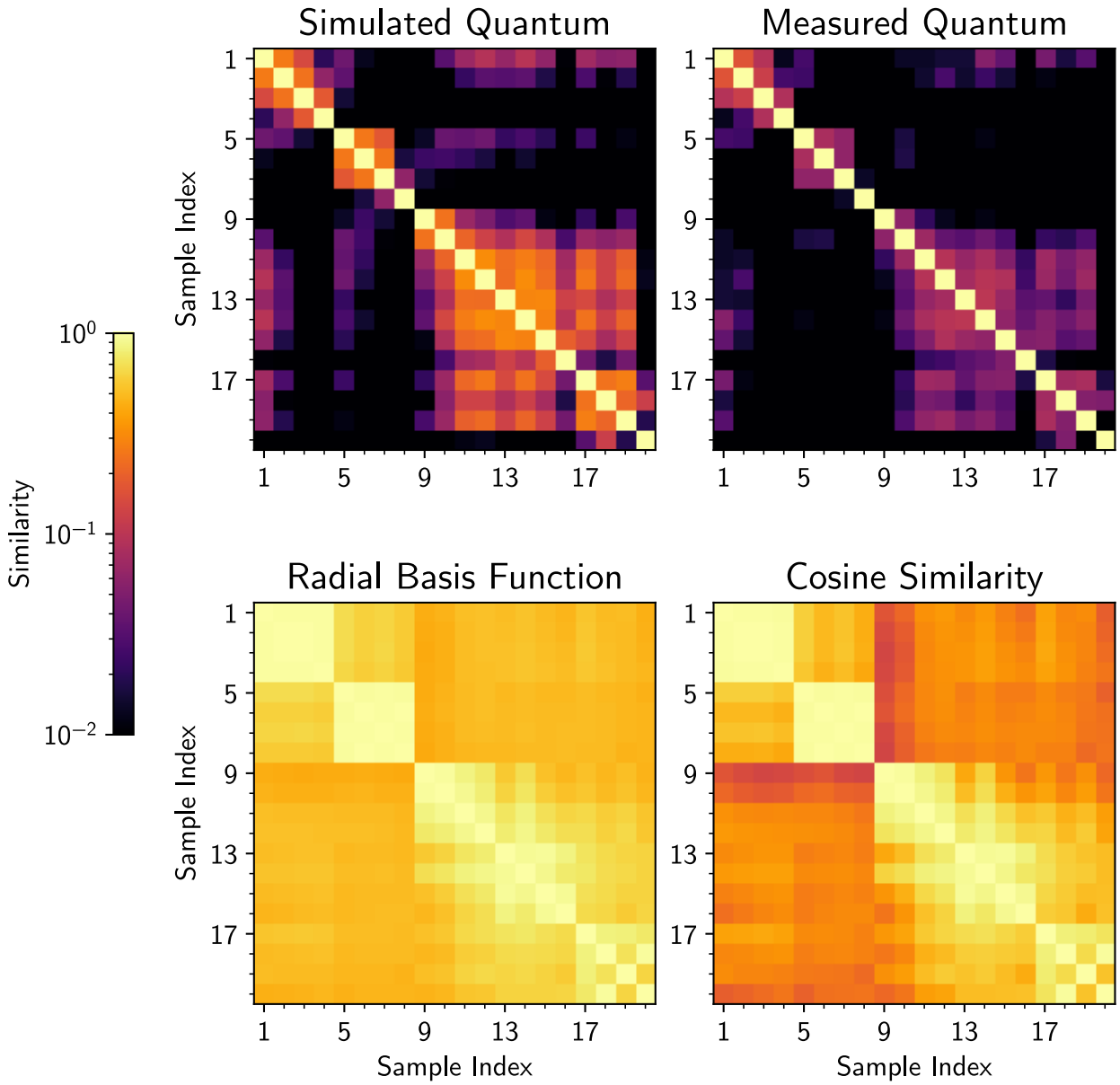



Figure A.1: A re-plot of the kernel matrices, all with the logarithmic scale.

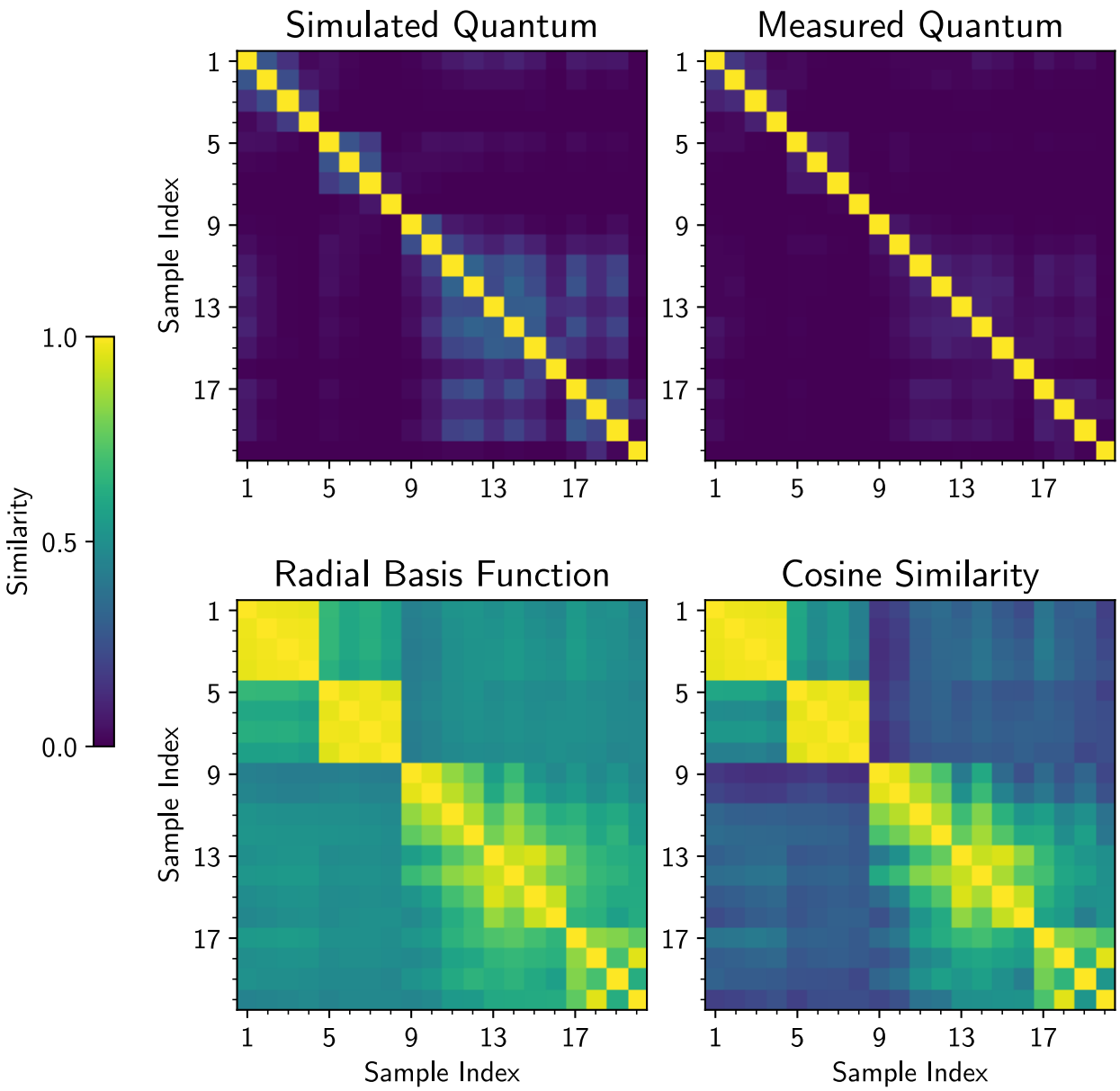



Figure A.2: A re-plot of the kernel matrices, all with the linear scale.

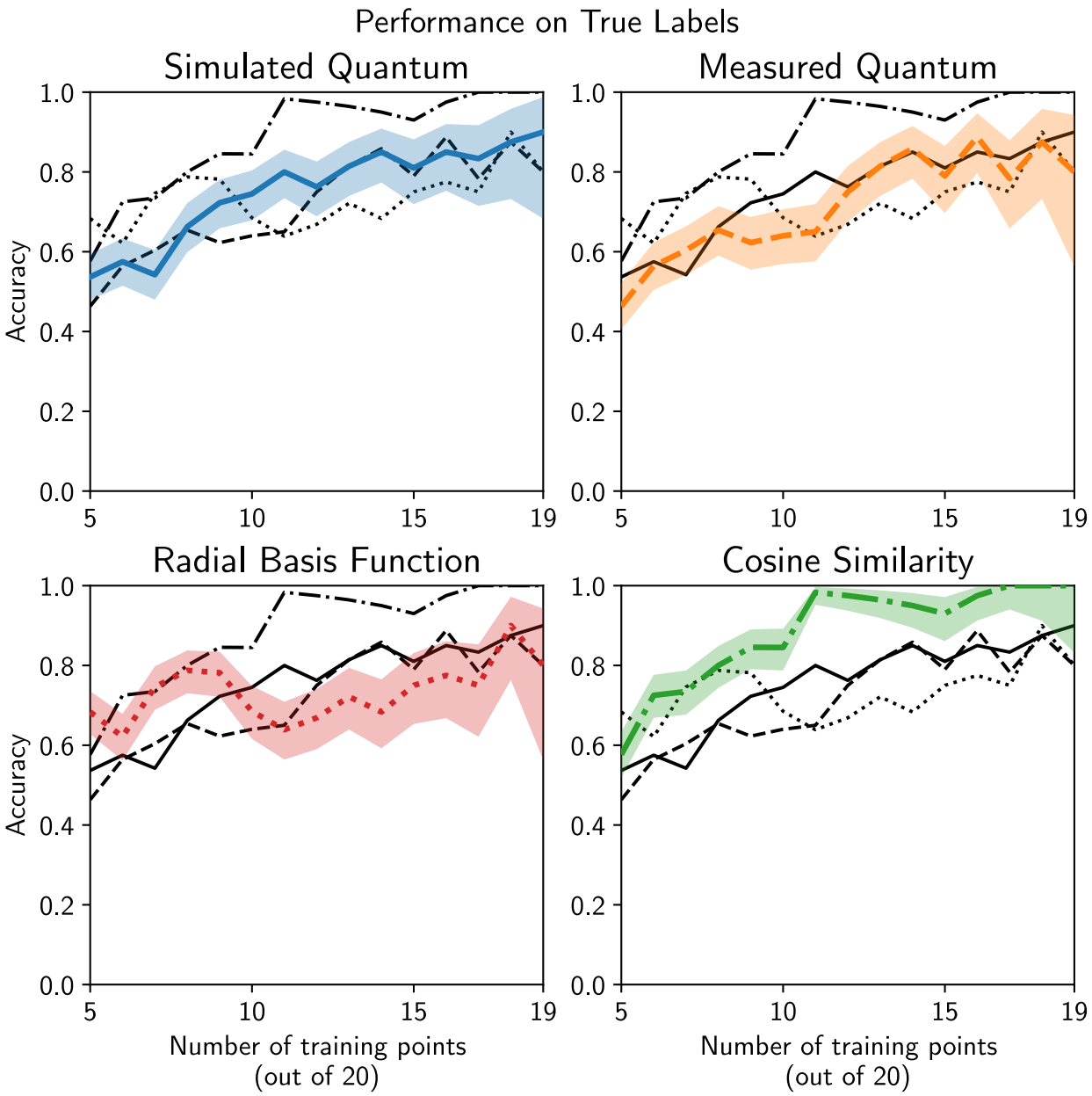



Figure A.3: The absolute accuracy of each of the kernels, as opposed to the relative accuracy of the quantum kernel, on the material science supervised learning task.

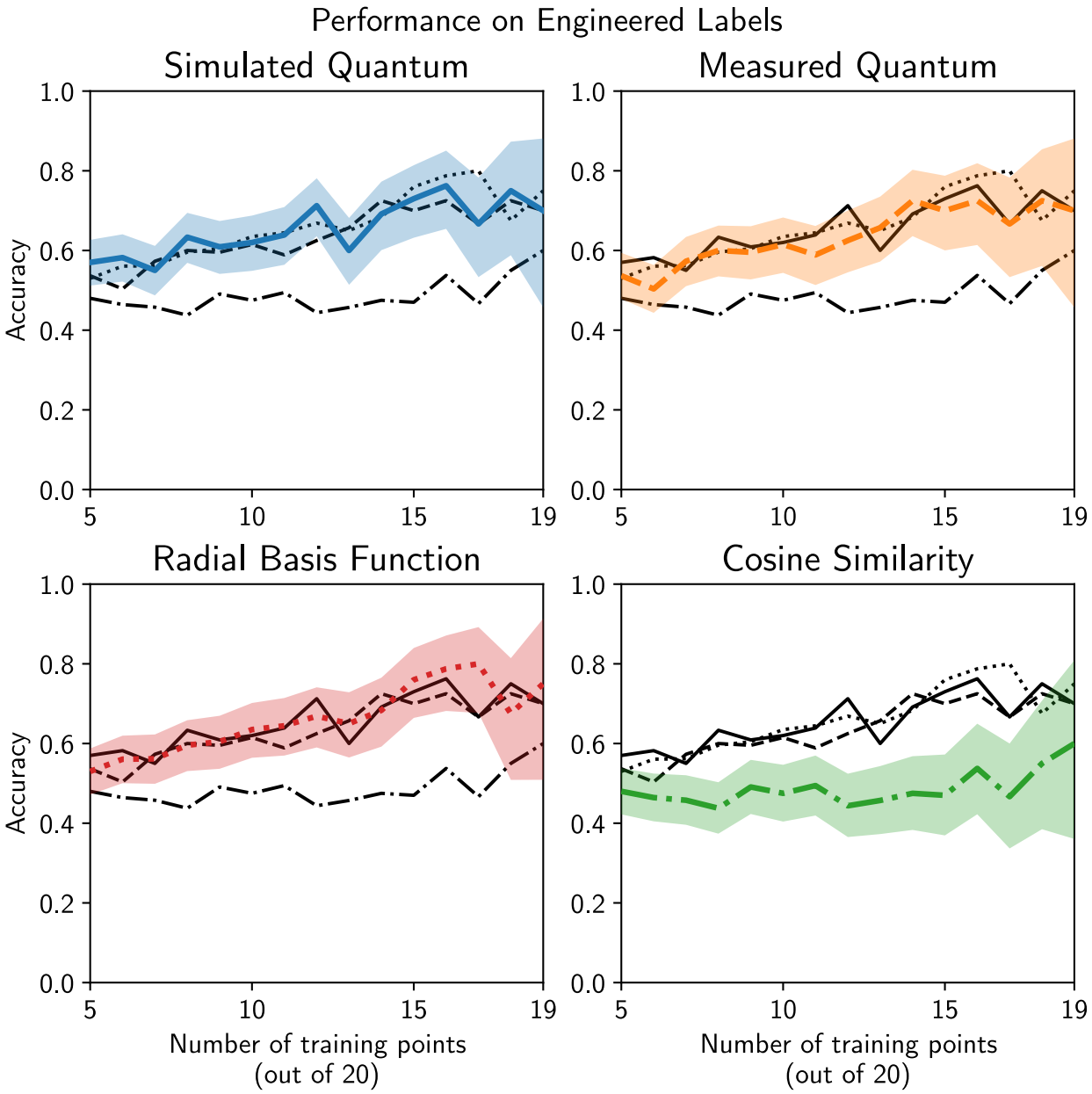



Figure A.4: The absolute accuracy of each of the kernels, as opposed to the relative accuracy of the quantum kernel, on the engineered label supervised learning task.

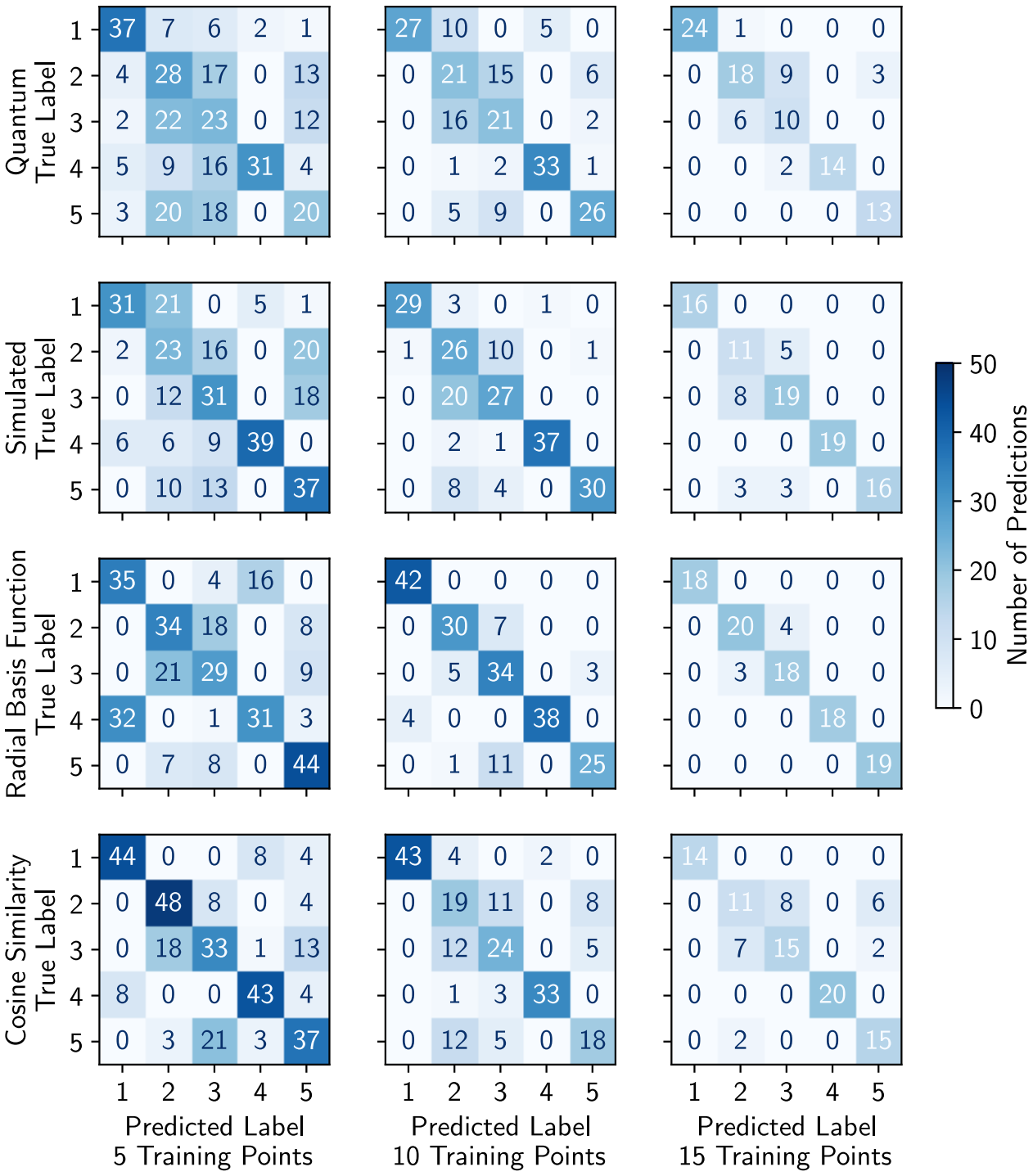



Figure A.5: Some confusion matrices for the materials science supervised learning task. The above confusion matrices are the sum of the 20 confusion matrices for each random training set sample.

# Appendix B: Supplementary Information for First-Principles Thermodynamic Analysis of Ternary Chalcogenide Phase Change Materials

## B.1 Results for Additional Select Mixtures

### B.1.1 In – Se Mixtures

InSe – $Bi_2Se_3$ mixtures have high energy near or above 50 meV / atom, indicating likely phase separation. InSe – $SiSe_2$ behaves similarly to most of the other $SiSe_2$ mixtures: most compositions are high in energy, but some specific compositions have negative energy above hull. This indicates that InSe – $SiSe_2$ mixtures are also compositionally and structurally inflexible and thus don't meet our criteria for a promising PCM candidate. Neither mixture appears in the PCM literature.

The $In_2Se_3$ – $Bi_2Se_3$ system has two similar polymorphs close in energy between about 20 to 40 meV / atom. Of the pair of polymorphs, the $P\bar{3}m1$ $In_2Se_3$ polymorph isn't the lowest energy polymorph. So, as the composition gets closer to $In_2Se_3$, the P61 $In_2Se_3$ is more likely to appear. However, energy of this polymorph is high enough that there is likely a large range of compositions where the two $P\bar{3}m1$ polymorphs are dominant and the mixture is promising PCM candidate. $In_2Se_3$ – SnSe2 mixtures, however, are above 40 meV / atom and likely to simple phase segregate. Neither mixture appears in the PCM literature, although $In_2Se_3$ on its own has been explored [99].

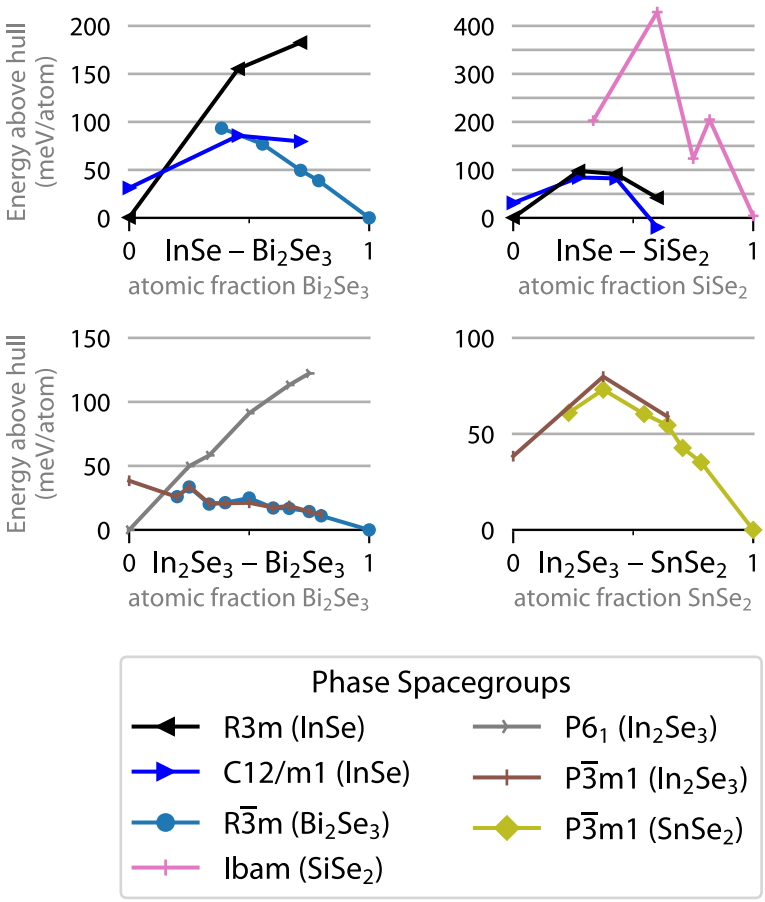



Figure B.1: The minimum DFT energies for structures in different phases as a function of composition for mixtures with In – Se binaries.

### B.1.2 Miscellaneous Mixtures

All of the GeTe – $Ga_2Te_3$ mixtures are above 50 meV / atom indicating phase segregation, in agreement with experimental measurements of the pseudobinary phase diagram [100]. The mixture doesn't appear in the PCM literature, but some experiments have been performed with $Ga_2Te_3$ on its own [101].

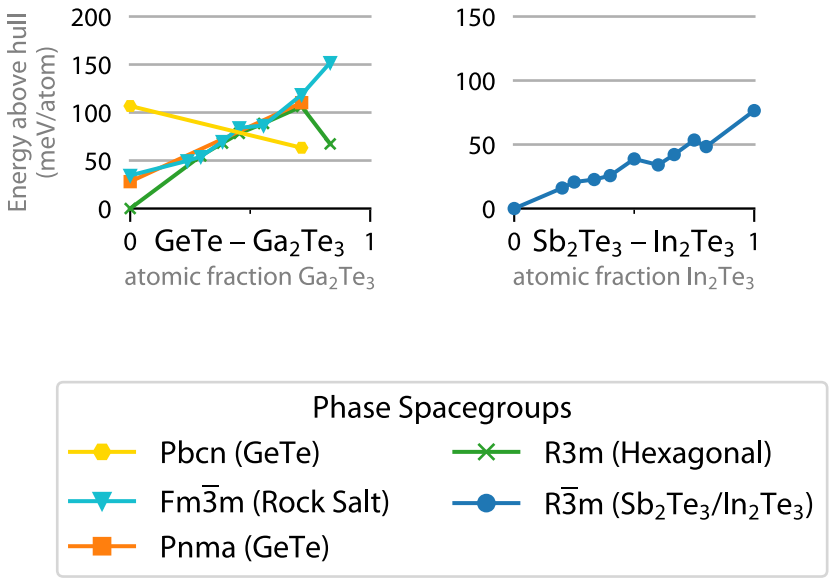



Figure B.2: The minimum DFT energies for structures in different phases as a function of composition for miscellaneous mixtures.

$Sb_2Te_3$ and $In_2Te_3$ share a common polymorph, but unlike $Sb_2Te_3$ – $Bi_2Te_3$, the R$\bar{3}$m polymorph isn't the lowest energy polymorph of $In_2Te_3$. This causes the energy of the mixtures to trend upward, up to 50 meV / atom, indicating the mixture is less stable as the concentration of $In_2Te_3$ increases. In practice, doping $Sb_{70}Te_{30}$ with small amounts (< 10 at. %) of In is used to create AIST, another well performing PCM.

# Bibliography


[1] Tony Hey, Stewart Tansley, Kristin Tolle, and Jim Gray. *The Fourth Paradigm: Data-Intensive Scientific Discovery*. Microsoft Research, October 2009.

[2] Materials Genome Initiative Strategic Plan. Technical report, US National Science and Technology Council, November 2021.

[3] M. L. Green, C. L. Choi, J. R. Hattrick-Simpers, A. M. Joshi, I. Takeuchi, S. C. Barron, E. Campo, T. Chiang, S. Empedocles, J. M. Gregoire, A. G. Kusne, J. Martin, A. Mehta, K. Persson, Z. Trautt, J. Van Duren, and A. Zakutayev. Fulfilling the promise of the materials genome initiative with high-throughput experimental methodologies. *Applied Physics Reviews*, 4(1):011105, 03 2017.

[4] Stefano Curtarolo, Gus L. W. Hart, Marco Buongiorno Nardelli, Natalio Mingo, Stefano Sanvito, and Ohad Levy. The high-throughput highway to computational materials design. *Nature Materials*, 12(3):191–201, March 2013.

[5] Eric Stach, Brian DeCost, A. Gilad Kusne, Jason Hattrick-Simpers, Keith A. Brown, Kristofer G. Reyes, Joshua Schrier, Simon Billinge, Tonio Buonassisi, Ian Foster, Carla P. Gomes, John M. Gregoire, Apurva Mehta, Joseph Montoya, Elsa Olivetti, Chiwoo Park, Eli Rotenberg, Semion K. Saikin, Sylvia Smullin, Valentin Stanev, and Benji Maruyama. Autonomous experimentation systems for materials development: A community perspective. *Matter*, 4(9):2702–2726, September 2021.

[6] Burr Settles. *Active Learning*. Synthesis Lectures on Artificial Intelligence and Machine Learning. Springer International Publishing, Cham, 2012.

[7] A. Gilad Kusne, Heshan Yu, Changming Wu, Huairuo Zhang, Jason Hattrick-Simpers, Brian DeCost, Suchismita Sarker, Corey Oses, Cormac Toher, Stefano Curtarolo, Albert V. Davydov, Ritesh Agarwal, Leonid A. Bendersky, Mo Li, Apurva Mehta, and Ichiro Takeuchi. On-the-fly closed-loop materials discovery via Bayesian active learning. *Nature Communications*, 11(1):5966, November 2020. Number: 1.

[8] Felix Adams, Austin McDannald, Ichiro Takeuchi, and A. Gilad Kusne. Human-in-the-loop for Bayesian autonomous materials phase mapping. *Matter*, 7(2):697–709, February 2024.

[9] Pavel Nikolaev, Daylond Hooper, Frederick Webber, Rahul Rao, Kevin Decker, Michael Krein, Jason Poleski, Rick Barto, and Benji Maruyama. Autonomy in materials research: a case study in carbon nanotube growth. *npj Computational Materials*, 2(1):1–6, October 2016. Number: 1.

[10] B. P. MacLeod, F. G. L. Parlane, T. D. Morrissey, F. Häse, L. M. Roch, K. E. Dettelbach, R. Moreira, L. P. E. Yunker, M. B. Rooney, J. R. Deeth, V. Lai, G. J. Ng, H. Situ, R. H.

Zhang, M. S. Elliott, T. H. Haley, D. J. Dvorak, A. Aspuru-Guzik, J. E. Hein, and C. P. Berlinguette. Self-driving laboratory for accelerated discovery of thin-film materials. *Science Advances*, 6(20):eaaz8867, May 2020.

[11] Austin McDannald, Matthias Frontzek, Andrei T. Savici, Mathieu Doucet, Efrain E. Rodriguez, Kate Meuse, Jessica Opsahl-Ong, Daniel Samarov, Ichiro Takeuchi, William Ratcliff, and A. Gilad Kusne. On-the-fly autonomous control of neutron diffraction via physics-informed Bayesian active learning. *Applied Physics Reviews*, 9(2):021408, April 2022.

[12] Sebastian Ament, Maximilian Amsler, Duncan R. Sutherland, Ming-Chiang Chang, Dan Guevarra, Aine B. Connolly, John M. Gregoire, Michael O. Thompson, Carla P. Gomes, and R. Bruce van Dover. Autonomous materials synthesis via hierarchical active learning of nonequilibrium phase diagrams. *Science Advances*, 7(51):eabg4930, December 2021.

[13] Helge S. Stein and John M. Gregoire. Progress and prospects for accelerating materials science with automated and autonomous workflows. *Chemical Science*, 10(42):9640–9649, 2019.

[14] Eduardo Mosqueira-Rey, Elena Hernández-Pereira, David Alonso-Ríos, José Bobes-Bascarán, and Ángel Fernández-Leal. Human-in-the-loop machine learning: a state of the art. *Artificial Intelligence Review*, 56(4):3005–3054, April 2023.

[15] JC Licklider. Man–computer symbiosis. *IRE Transactions on Human Factors in Electronics*, pages 4–11, 1960.

[16] Ben Shneiderman. Human-centered artificial intelligence: Reliable, safe & trustworthy. *International Journal of Human-Computer Interaction*, 36(6):495–504, 2020.

[17] Jingda Wu, Zhiyu Huang, Zhongxu Hu, and Chen Lv. Toward human-in-the-loop ai: Enhancing deep reinforcement learning via real-time human guidance for autonomous driving. *Engineering*, 21:75–91, 2023.

[18] Lu Feng, Clemens Wiltsche, Laura Humphrey, and Ufuk Topcu. Synthesis of human-in-the-loop control protocols for autonomous systems. *IEEE Transactions on Automation Science and Engineering*, 13(2):450–462, 2016.

[19] Eduard Fosch-Villaronga, Pranav Khanna, Hadassah Drukarch, and Bart H. M. Custers. A human in the loop in surgery automation. *Nature Machine Intelligence*, 3:368–369, 2021.

[20] Prajit T. Rajendran, Huascar Espinoza, Agnes Delaborde, and Chokri Mraidha. Human-in-the-loop learning methods toward safe dl-based autonomous systems: A review. In Ibrahim Habli, Mark Sujan, Simos Gerasimou, Erwin Schoitsch, and Friedemann Bitsch, editors, *Computer Safety, Reliability, and Security. SAFECOMP 2021 Workshops*, pages 251–264, Cham, 2021. Springer International Publishing.

[21] Dezhen Xue, Prasanna V. Balachandran, John Hogden, James Theiler, Deqing Xue, and Turab Lookman. Accelerated search for materials with targeted properties by adaptive design. *Nature Communications*, 7(1):11241, April 2016. Number: 1.

[22] Cheng Wen, Yan Zhang, Changxin Wang, Dezhen Xue, Yang Bai, Stoichko Antonov, Lanhong Dai, Turab Lookman, and Yanjing Su. Machine learning assisted design of high entropy alloys with desired property. *Acta Materialia*, 170:109–117, 2019.

[23] Shijing Sun, Noor T. P. Hartono, Zekun D. Ren, Felipe Oviedo, Antonio M. Buscemi, Mariya Layurova, De Xin Chen, Tofunmi Ogunfunmi, Janak Thapa, Savitha Ramasamy, Charles Settens, Brian L. DeCost, Aaron G. Kusne, Zhe Liu, Siyu I. P. Tian, Ian Marius Peters, Juan-Pablo Correa-Baena, and Tonio Buonassisi. Accelerated Development of Perovskite-Inspired Materials via High-Throughput Synthesis and Machine-Learning Diagnosis. *Joule*, 3(6):1437–1451, June 2019.

[24] Ronan Le Bras, Richard Bernstein, Carla P. Gomes, Bart Selman, and R. Bruce Van Dover. Crowdsourcing backdoor identification for combinatorial optimization. In *Proceedings of the Twenty-Third international joint conference on Artificial Intelligence*, IJCAI '13, pages 2840–2847, Beijing, China, August 2013. AAAI Press.

[25] A. Gilad Kusne, Austin McDannald, Brian DeCost, Corey Oses, Cormac Toher, Stefano Curtarolo, Apurva Mehta, and Ichiro Takeuchi. Physics in the Machine: Integrating Physical Knowledge in Autonomous Phase-Mapping. *Frontiers in Physics*, 10:815863, February 2022. arXiv:2111.07478 [cond-mat].

[26] Carl Edward Rasmussen and Christopher K. I. Williams. *Gaussian processes for machine learning*. Adaptive computation and machine learning. MIT Press, Cambridge, Mass., 3. print edition, 2008.

[27] C. J. Long, J. Hattrick-Simpers, M. Murakami, R. C. Srivastava, I. Takeuchi, V. L. Karen, and X. Li. Rapid structural mapping of ternary metallic alloy systems using the combinatorial approach and cluster analysis. *Review of Scientific Instruments*, 78(7):072217, July 2007.

[28] E. B. Fowlkes and C. L. Mallows. A Method for Comparing Two Hierarchical Clusterings. *Journal of the American Statistical Association*, 78(383):553–569, 1983.

[29] A. G. Kusne, D. Keller, A. Anderson, A. Zaban, and I. Takeuchi. High-throughput determination of structural phase diagram and constituent phases using GRENDEL. *Nanotechnology*, 26(44):444002, October 2015.

[30] H. B. Mann and D. R. Whitney. On a Test of Whether one of Two Random Variables is Stochastically Larger than the Other. *The Annals of Mathematical Statistics*, 18(1):50–60, 1947.

[31] Felix Adams, Daiwei Zhu, David W. Steuerman, A. Gilad Kusne, and Ichiro Takeuchi. Quantum kernel machine learning for autonomous materials science. *APL Quantum*, 3(1):016115, 03 2026.

[32] Martin Seifrid, Robert Pollice, Andrés Aguilar-Granda, Zamyla Morgan Chan, Kazuhiro Hotta, Cher Tian Ser, Jenya Vestfrid, Tony C. Wu, and Alán Aspuru-Guzik. Autonomous Chemical Experiments: Challenges and Perspectives on Establishing a Self-Driving Lab. *Accounts of Chemical Research*, 55(17):2454–2466, September 2022.

[33] Milad Abolhasani and Eugenia Kumacheva. The rise of self-driving labs in chemical and materials sciences. *Nature Synthesis*, 2(6):483–492, June 2023.

[34] Nathan J. Szymanski, Pragnay Nevatia, Christopher J. Bartel, Yan Zeng, and Gerbrand Ceder. Autonomous and dynamic precursor selection for solid-state materials synthesis. *Nature Communications*, 14(1):6956, October 2023.

[35] Martin L. Green, Ichiro Takeuchi, and Jason R. Hattrick-Simpers. Applications of high throughput (combinatorial) methodologies to electronic, magnetic, optical, and energy-related materials. *Journal of Applied Physics*, 113(23):231101, June 2013.

[36] Archit Parnami and Minwoo Lee. Learning from Few Examples: A Summary of Approaches to Few-Shot Learning, March 2022. arXiv:2203.04291 [cs].

[37] Alexander G. de G. Matthews, Mark van der Wilk, Tom Nickson, Keisuke Fujii, Alexis Boukouvalas, Pablo León-Villagrá, Zoubin Ghahramani, and James Hensman. GPflow: A Gaussian Process Library using TensorFlow. *Journal of Machine Learning Research*, 18(40):1–6, 2017.

[38] Hsin-Yuan Huang, Michael Broughton, Masoud Mohseni, Ryan Babbush, Sergio Boixo, Hartmut Neven, and Jarrod R. McClean. Power of data in quantum machine learning. *Nature Communications*, 12(1):2631, May 2021. Number: 1.

[39] D.H. Wolpert and W.G. Macready. No free lunch theorems for optimization. *IEEE Transactions on Evolutionary Computation*, 1(1):67–82, April 1997.

[40] Charles Kittel. *Introduction to solid state physics*. Wiley, Hoboken, NJ, 8. ed., [repr.] edition, 2004.

[41] Aram W. Harrow, Avinatan Hassidim, and Seth Lloyd. Quantum Algorithm for Linear Systems of Equations. *Physical Review Letters*, 103(15):150502, October 2009.

[42] Maicon Pierre Lourenço, Hadi Zadeh-Haghighi, Jiří Hostaš, Mosayeb Naseri, Daya Gaur, Christoph Simon, and Dennis R. Salahub. Exploring Quantum Active Learning for Materials Design and Discovery, July 2024. arXiv:2407.18731 [quant-ph].

[43] I. Takeuchi, O. O. Famodu, J. C. Read, M. A. Aronova, K.-S. Chang, C. Craciunescu, S. E. Lofland, M. Wuttig, F. C. Wellstood, L. Knauss, and A. Orozco. Identification of novel compositions of ferromagnetic shape-memory alloys using composition spreads. *Nature Materials*, 2(3):180–184, March 2003.

[44] Riccardo Mengoni and Alessandra Di Pierro. Kernel methods in Quantum Machine Learning. *Quantum Machine Intelligence*, 1(3):65–71, December 2019.

[45] Yuma Iwasaki, A. Gilad Kusne, and Ichiro Takeuchi. Comparison of dissimilarity measures for cluster analysis of X-ray diffraction data from combinatorial libraries. *npj Computational Materials*, 3(1):1–9, February 2017.

[46] Michael A. Nielsen and Isaac L. Chuang. *Quantum computation and quantum information*. Cambridge University Press, Cambridge ; New York, 10th anniversary ed edition, 2010.

[47] Vojtěch Havlíček, Antonio D. Córcoles, Kristan Temme, Aram W. Harrow, Abhinav Kandala, Jerry M. Chow, and Jay M. Gambetta. Supervised learning with quantum-enhanced feature spaces. *Nature*, 567(7747):209–212, March 2019. Number: 7747.

[48] Evan Peters, João Caldeira, Alan Ho, Stefan Leichenauer, Masoud Mohseni, Hartmut Neven, Panagiotis Spentzouris, Doug Strain, and Gabriel N. Perdue. Machine learning of high dimensional data on a noisy quantum processor, January 2021. arXiv:2101.09581 [quant-ph].

[49] Andrea Skolik, Michele Cattelan, Sheir Yarkoni, Thomas Bäck, and Vedran Dunjko. Equivariant quantum circuits for learning on weighted graphs. *npj Quantum Information*, 9(1):47, May 2023.

[50] Koki Chinzei, Quoc Hoan Tran, Kazunori Maruyama, Hirotaka Oshima, and Shintaro Sato. Splitting and parallelizing of quantum convolutional neural networks for learning translationally symmetric data. *Physical Review Research*, 6(2):023042, April 2024.

[51] Patrick Rebentrost, Masoud Mohseni, and Seth Lloyd. Quantum Support Vector Machine for Big Data Classification. *Physical Review Letters*, 113(13):130503, September 2014.

[52] Maria Schuld and Nathan Killoran. Quantum Machine Learning in Feature Hilbert Spaces. *Physical Review Letters*, 122(4):040504, February 2019.

[53] D. Katz, J. Baptista, S. P. Azen, and M. C. Pike. Obtaining Confidence Intervals for the Risk Ratio in Cohort Studies. *Biometrics*, 34(3):469–474, 1978.

[54] C. J. Long, D. Bunker, X. Li, V. L. Karen, and I. Takeuchi. Rapid identification of structural phases in combinatorial thin-film libraries using x-ray diffraction and non-negative matrix factorization. *Review of Scientific Instruments*, 80(10):103902, October 2009.

[55] Tom M. Mitchell. *Machine learning*. McGraw-Hill series in Computer Science. McGraw-Hill, New York, 1997.

[56] Ulrike von Luxburg and Bernhard Schoelkopf. Statistical Learning Theory: Models, Concepts, and Results, October 2008. arXiv:0810.4752 [stat].

[57] Brian Kulis. Metric Learning: A Survey. *Foundations and Trends® in Machine Learning*, 5(4):287–364, 2013.

[58] Andrea Redaelli, editor. *Phase Change Memory*. Springer International Publishing, Cham, 2018.

[59] Simone Raoux and Matthias Wuttig, editors. *Phase Change Materials*. Springer US, Boston, MA, 2009.

[60] M. Wuttig, H. Bhaskaran, and T. Taubner. Phase-change materials for non-volatile photonic applications. *Nature Photonics*, 11(8):465–476, August 2017. Number: 8.

[61] Noboru Yamada. Origin, secret, and application of the ideal phase-change material GeSbTe. *physica status solidi (b)*, 249(10):1837–1842, 2012. _eprint: https://onlinelibrary.wiley.com/doi/pdf/10.1002/pssb.201200618.

[62] W. Ostwald. Studien über die Bildung und Umwandlung fester Körper: 1. Abhandlung: Übersättigung und Überkaltung. *Zeitschrift für Physikalische Chemie*, 22U(1):289–330, February 1897.

[63] Terry Threlfall. Structural and Thermodynamic Explanations of Ostwald's Rule. *Organic Process Research & Development*, 7(6):1017–1027, November 2003.

[64] S. Caravati, M. Bernasconi, T. D. Kühne, M. Krack, and M. Parrinello. First-principles study of crystalline and amorphous Ge2Sb2Te5 and the effects of stoichiometric defects. *Journal of Physics: Condensed Matter*, 21(25):255501, June 2009.

[65] Juarez L. F. Da Silva, Aron Walsh, and Hosun Lee. Insights into the structure of the stable and metastable ( GeTe ) m ( Sb 2 Te 3 ) n compounds. *Physical Review B*, 78(22):224111, December 2008.

[66] Tae-Yon Lee, Cheolkyu Kim, Younseon Kang, Dong-Seok Suh, Kijoon H. P. Kim, and Yoonho Khang. Rapid crystallization of GeTe-Bi2Te3 mixed layer. *Applied Physics Letters*, 92(10):101908, March 2008.

[67] J. N Bierly, L Muldawer, and O Beckman. The continuous rhombohedral-gubic transformation in GeTe-SnTe alloys. *Acta Metallurgica*, 11(5):447–454, May 1963.

[68] Christoph Persch, Maximilian J. Müller, Aakash Yadav, Julian Pries, Natalie Honné, Peter Kerres, Shuai Wei, Hajime Tanaka, Paolo Fantini, Enrico Varesi, Fabio Pellizzer, and Matthias Wuttig. The potential of chemical bonding to design crystallization and vitrification kinetics. *Nature Communications*, 12(1):4978, August 2021.

[69] Mac J. Smith, R. J. Knight, and C. W. Spencer. Properties of Bi2Te3-Sb2Te3 Alloys. *Journal of Applied Physics*, 33(7):2186–2190, July 1962.

[70] O Pagès, Y Feutelais, J.R Didry, G Keller, H Jacquemin, and B Legendre. Phase change optical recording films based on Bi2Te3-Sb2Te3 alloys. *Materials Research Bulletin*, 34(7):1065–1077, May 1999.

[71] Aynur E. Seidzade, Elnur N. Orujlu, Thomas Doert, Imamaddin R. Amiraslanov, Ziya S. Aliev, and Mahammad B. Babanly. An Updated Phase Diagram of the SnTe-Sb2Te3 System and the Crystal Structure of the New Compound SnSb4Te7. *Journal of Phase Equilibria and Diffusion*, 42(3):373–378, June 2021.

[72] Bryan A. Kuropatwa and Holger Kleinke. Thermoelectric Properties of Stoichiometric Compounds in the (SnTe)x(Bi2Te3)y System. *Zeitschrift für anorganische und allgemeine Chemie*, 638(15):2640–2647, 2012. _eprint: https://onlinelibrary.wiley.com/doi/pdf/10.1002/zaac.201200284.

[73] Susumu Soeya, Toshimichi Shintani, Takahiro Odaka, Reiko Kondou, and Junji Tominaga. Ultra-low switching power, crystallographic analysis, and switching mechanism for SnXTe100-X/Sb2Te3 diluted superlattice system. *Applied Physics Letters*, 103(5), July 2013.

[74] Pavla Honcová, Diego Valdés, Jaroslav Barták, Jiri Málek, Petr Pilný, and Stanislav Slang. Combination of indirect and direct approaches to the description of complex crystallization behavior in GeSe2-rich region of pseudobinary GeSe2-Sb2Se3 system. *Journal of Non-Crystalline Solids*, 568:120968, September 2021.

[75] V. Vassilev, K. Tomova, V. Parvanova, and S. Boycheva. Glass-formation in the GeSe2-Sb2Se3-SnSe system. *Journal of Alloys and Compounds*, 485(1-2):569–572, October 2009.

[76] Didarul Islam and R. L. Cappelletti. Structural evolution during annealing of laser-ablation-deposited Ge-Sn-Se amorphous films. *Physical Review B*, 44(6):2516–2522, August 1991.

[77] Kristy A. Campbell and Christopher M. Anderson. Phase-change memory devices with stacked Ge-chalcogenide/Sn-chalcogenide layers. *Microelectronics Journal*, 38(1):52–59, January 2007.

[78] E. N. Ismailova, L. F. Mashadieva, D. M. Babanly, A. V. Shevel'kov, and M. B. Babanly. Diagram of Solid-Phase Equilibria in the SnSe-Sb2Se3-Se System and Thermodynamic Properties of Tin Antimony Selenides. *Russian Journal of Inorganic Chemistry*, 66(1):96–103, January 2021.

[79] Jiyu Li, Bo Wang, Fangyang Liu, Jun Liu, Ming Jia, Yanqing Lai, Jie Li, and Yexiang Liu. Structural and Optical Properties of Electrodeposited Bi2-xSbxSe3 Thin Films. *ECS Solid State Letters*, 1(3):Q29, August 2012.

[80] J. Feng, Y. Zhang, B.W. Qiao, Y.F. Lai, Y.Y. Lin, B.C. Cai, T.A. Tang, and B. Chen. Si doping in Ge2Sb2Te5 film to reduce the writing current of phase change memory. *Applied Physics A*, 87(1):57–62, April 2007.

[81] Chih-Yu Lee, Yi-Siou Huang, Felix Adams, Chuanyu Lian, Hongyi Sun, Jie Zhao, Zichao Ye, Nathan Youngblood, Juejun Hu, Leslie H Allen, Yifei Mo, Ichiro Takeuchi, and Carlos A Ríos Ocampo. Incorporating Si into Sb2Se3: Tailoring Optical Phase Change Materials via Nanocomposites. *Advanced Optical Materials*, 14(8):e03389, 2026.

[82] A. A. Kozma, M. Yu. Sabov, E. Yu. Peresh, I. E. Barchiy, and V. V. Tsygyka. Thermoelectric properties of a eutectic SnSe2-Bi2Se3 alloy. *Inorganic Materials*, 51(2):93–97, February 2015.

[83] Frank Heinke, Philipp Urban, Anton Werwein, Christina Fraunhofer, Tobias Rosenthal, Stefan Schwarzmüller, Daniel Souchay, Felix Fahrnbauer, Vadim Dyadkin, Gerald Wagner, and Oliver Oeckler. Cornucopia of Structures in the Pseudobinary System (SnSe)xBi2Se3: A Crystal-Chemical Copycat. *Inorganic Chemistry*, 57(8):4427–4440, April 2018.

[84] A.M. Adam, A.K. Diab, Mohamed Tolan, Z.M.H. El-Qahtani, A.A. Refaat, Medhat A. El-Hadek, E.M. Elsehly, A. El-Khouly, Abdulaziz N. Alharbi, V. Khovaylo, and M. Ataalla. Outstanding optical properties of thermally grown (Bi2Se3)1-x (Bi2Te3)x thin films. *Materials Science in Semiconductor Processing*, 143:106557, June 2022.

[85] Fouad Abdel-Wahab. Observation of phase separation in some Se-Te-Sn chalcogenide glasses. *Physica B: Condensed Matter*, 406(5):1053–1059, March 2011.

[86] Simon Divilov, Hagen Eckert, David Hicks, Corey Oses, Cormac Toher, Rico Friedrich, Marco Esters, Michael J. Mehl, Adam C. Zettel, Yoav Lederer, Eva Zurek, Jon-Paul Maria, Donald W. Brenner, Xiomara Campilongo, Suzana Filipović, William G. Fahrenholtz, Caillin J. Ryan, Christopher M. DeSalle, Ryan J. Crealese, Douglas E. Wolfe, Arrigo Calzolari, and Stefano Curtarolo. Disordered enthalpy-entropy descriptor for high-entropy ceramics discovery. *Nature*, 625(7993):66–73, January 2024. Number: 7993.

[87] D. De Fontaine. Cluster approach to order-disorder transformations in alloys. volume 47 of *Solid State Physics*, pages 33–176. Academic Press, 1994.

[88] J. Hegedüs and S. R. Elliott. Microscopic origin of the fast crystallization ability of Ge-Sb-Te phase-change memory materials. *Nature Materials*, 7(5):399–405, May 2008.

[89] Yazhi Xu, Yuxing Zhou, Xu-Dong Wang, Wei Zhang, En Ma, Volker L. Deringer, and Riccardo Mazzarello. Unraveling crystallization mechanisms and electronic structure of phase-change materials by large-scale ab initio simulations. *Advanced Materials*, 34(11):2109139, 2022.

[90] Anubhav Jain, Shyue Ping Ong, Geoffroy Hautier, Wei Chen, William Davidson Richards, Stephen Dacek, Shreyas Cholia, Dan Gunter, David Skinner, Gerbrand Ceder, and Kristin A. Persson. Commentary: The Materials Project: A materials genome approach to accelerating materials innovation. *APL Materials*, 1(1):011002, July 2013.

[91] Anubhav Jain, Geoffroy Hautier, Charles J. Moore, Shyue Ping Ong, Christopher C. Fischer, Tim Mueller, Kristin A. Persson, and Gerbrand Ceder. A high-throughput infrastructure for density functional theory calculations. *Computational Materials Science*, 50(8):2295–2310, June 2011.

[92] Shyue Ping Ong, Lei Wang, Byoungwoo Kang, and Gerbrand Ceder. Li-Fe-P-O2 Phase Diagram from First Principles Calculations. *Chemistry of Materials*, 20(5):1798–1807, March 2008.

[93] Shyue Ping Ong, Anubhav Jain, Geoffroy Hautier, Byoungwoo Kang, and Gerbrand Ceder. Thermal stabilities of delithiated olivine MPO4 (M=Fe, Mn) cathodes investigated using first principles calculations. *Electrochemistry Communications*, 12(3):427–430, March 2010.

[94] Peter E. Hart, Nils J. Nilsson, and Bertram Raphael. A Formal Basis for the Heuristic Determination of Minimum Cost Paths. *IEEE Transactions on Systems Science and Cybernetics*, 4(2):100–107, July 1968.

[95] James W. Furness, Aaron D. Kaplan, Jinliang Ning, John P. Perdew, and Jianwei Sun. Accurate and Numerically Efficient r2SCAN Meta-Generalized Gradient Approximation. *The Journal of Physical Chemistry Letters*, 11(19):8208–8215, October 2020.

[96] Gus L. W. Hart and Rodney W. Forcade. Algorithm for generating derivative structures. *Physical Review B*, 77(22):224115, June 2008.

[97] John P. Perdew, Kieron Burke, and Matthias Ernzerhof. Generalized Gradient Approximation Made Simple. *Physical Review Letters*, 77(18):3865–3868, October 1996.

[98] G. Kresse and J. Hafner. Ab initio molecular dynamics for liquid metals. *Physical Review B*, 47(1):558–561, January 1993.

[99] Heon Lee, Dae-Hwan Kang, and Lung Tran. Indium selenide (In2Se3) thin film for phase-change memory. *Materials Science and Engineering: B*, 119(2):196–201, May 2005.

[100] N. Kh Abrikosov, G. T. Danilova-Dobryakova, and R. V. Shalamberidze. Investigation into GeTe-Ga2Te3 system. 12(4):605–609, April 1976.

[101] Hao Zhu, Jiang Yin, Yidong Xia, and Zhiguo Liu. Ga2Te3 phase change material for low-power phase change memory application. *Applied Physics Letters*, 97(8):083504, August 2010.